



Li, W., Grech, J., Stortz, J. F., Gow, M., Periz, J., Meissner, M. and Jimenez-Ruiz, E. (2022) A splitCas9 phenotypic screen in *Toxoplasma gondii* identifies proteins involved in host cell egress and invasion. *Nature Microbiology*, 7(6), pp. 882-895.  
(doi: [10.1038/s41564-022-01114-y](https://doi.org/10.1038/s41564-022-01114-y))

There may be differences between this version and the published version.  
You are advised to consult the published version if you wish to cite from it.

<http://eprints.gla.ac.uk/271254/>

Deposited on 29 June 2022

Enlighten – Research publications by members of the University of Glasgow  
<http://eprints.gla.ac.uk>

1 **A splitCas9 phenotypic screen in *Toxoplasma gondii* identifies proteins**  
2 **involved in host cell egress and invasion**

3

4 Wei Li<sup>1#</sup>, Janessa Grech<sup>1#</sup>, Johannes Felix Stortz<sup>2,3#</sup>, Matthew Gow<sup>1</sup>, Javier Periz<sup>1</sup>, Markus  
5 Meissner<sup>1,2\*</sup> and Elena Jimenez-Ruiz<sup>1\*</sup>

6

7 <sup>1</sup> Experimental Parasitology, Department of Veterinary Sciences, Faculty of Veterinary  
8 Medicine, Ludwig-Maximilians-Universität, LMU. Munich, Germany.

9 <sup>2</sup> Wellcome Centre for Integrative Parasitology, Institute of Infection, Immunity &  
10 Inflammation, Glasgow Biomedical Research Centre, University of Glasgow, Glasgow,  
11 United Kingdom.

12 <sup>3</sup> Max Planck Institute for Biology of Ageing, Cologne, Germany

13

14

15 \* Corresponding authors: M.M.: [Markus.meissner@para.vetmed.uni-muenchen.de](mailto:Markus.meissner@para.vetmed.uni-muenchen.de) ; E.J.R.:  
16 [Elena.jimenez@para.vetmed.uni-muenchen.de](mailto:Elena.jimenez@para.vetmed.uni-muenchen.de)

17

18 # Equal contribution

19

20 **Abstract**

21 Apicomplexan parasites, such as *Toxoplasma gondii*, have specific adaptations that enable  
22 invasion and exit from the host cell. Owing to the phylogenetic distance between  
23 apicomplexan parasites and model organisms, comparative genomics has limited capacity to  
24 infer gene functions. Further, although CRISPR/Cas9-based screens have assigned roles to  
25 some *Toxoplasma* genes, the functions of encoded proteins have proven difficult to assign.  
26 To overcome this problem, we devised a conditional Cas9-system in *T. gondii* that enables  
27 phenotypic screens. Using an indicator strain for F-actin dynamics and apicoplast  
28 segregation, we screened 320 genes to identify those required for defined steps in the  
29 asexual life-cycle. The detailed characterization of two genes identified in our screen,  
30 through the generation of conditional knockout parasites using the DiCre system, revealed  
31 that signalling linking factor (SLF) is an integral part of a signalling complex required for early  
32 induction of egress, and a novel conoid protein (conoid gliding protein, CGP) functions late  
33 during egress and is required for the activation of gliding motility. Establishing different  
34 indicator lines and applying our conditional Cas9 screen could enable the identification of  
35 genes involved in organellar biogenesis, parasite replication or maintenance of the  
36 endosymbiotic organelles in future.

37 **Main**

38 Apicomplexans are early branching eukaryotes related to ciliates and dinoflagellates, with  
39 unique adaptations to an intracellular, parasitic existence. The huge phylogenetic distance to  
40 well established model organisms is also reflected by the fact that many genes are unique  
41 and annotated as hypothetical. With the advancement of the CRISPR/Cas9 technology in *T.*  
42 *gondii*, genome-wide screens allowed the identification of genes that are important during the  
43 asexual stage of the parasite<sup>1</sup> with many hypothetical genes being critical for the survival of  
44 the parasite. While pooled screens allow the identification of fitness conferring genes,  
45 downstream assays are required to define functional groups based on the specific phenotype  
46 caused by their deletion.

47 A prerequisite for phenotypic screens in *T. gondii* is the use of conditional regulation systems  
48 in a high-throughput manner. We previously attempted to implement a conditional Cas9  
49 system based on ddFKBP, which suffered from inefficient regulation, prohibiting tight  
50 temporal control of Cas9 activity<sup>2</sup>. This resulted in non-essential genes being rapidly lost in a  
51 transfected pool (unpublished).

52 Here, we adapted a tight control system for Cas9, based on splitCas9 (sCas9)<sup>3</sup> and  
53 generated indicator parasites, expressing chromobodies directed against F-actin<sup>4</sup> and a  
54 marker for the apicoplast (FNR-RFP; a plastid like organelle) that allowed the identification of  
55 specific phenotypes in an image-based screen for parasites with abnormal invasion,  
56 replication and host cell egress and in parallel the characterisation of changes in F-actin  
57 dynamics and apicoplast segregation. We screened a curated library of 320 genes, with  
58 more than 40% annotated as hypothetical and conserved within the phylum of Apicomplexa<sup>1</sup>  
59 and grouped them into relevant phenotypes. Focusing on genes required for host cell egress,  
60 we identified and characterised a novel conoid associated protein (TGGT1\_240380) and a  
61 putative neurotransmitter symporter (TGGT1\_208420). Detailed analysis, using time lapse  
62 demonstrates that these genes are critical for distinct, independent steps that act at different  
63 times during host cell egress.

64

## 65 **Results**

### 66 *Adaptation of a conditional Cas9-system in T. gondii*

67 In order to achieve tight, temporal control of Cas9, we chose the sCas9 system<sup>3</sup>, where the  
68 Cas9 enzyme is split into two subunits (N- and C-terminus), which are fused to a FKBP and  
69 FRB domain. Upon addition of rapamycin these subunits interact and Cas9 activity is  
70 restored (Fig.1a). We generated transgenic RH $\Delta$ HX parasites expressing both sCas9  
71 subunits (Extended DataFig.1a,b), resulting in the recipient strain RHsCas9.

72 To test efficiency and specificity of this system, we generated vectors for stable expression of  
73 small guide RNAs (sgRNA) against previously described essential (*gap40*) and non-essential  
74 genes (*sag1*<sup>5</sup>). The critical function of the gliding associated protein 40 (GAP40) in assembly  
75 of the inner membrane complex (IMC) has been described previously<sup>6</sup>. The gRNA  
76 expression constructs were randomly integrated into the genome of RHsCas9 and into  
77 RH $\Delta$ HX parasites (Supplementary Table1; Extended DataFig.1c,d,e). Subsequently,  
78 parasites were induced with 50nM rapamycin for 1h or 48h before they were analysed.  
79 Induction of RHsCas9-*gap40*, but not RH-*gap40* or RHsCas9 parasites resulted in a severe  
80 replication defect (Fig.1b,c). Notably, deletion of *gap40* using the DiCre-system causes a  
81 similar phenotype, caused by the incomplete assembly of the IMC<sup>6</sup>. No difference in  
82 induction rate was observed upon 1 or 48 hours of rapamycin treatment, demonstrating that  
83 the sCas9 system allows efficient and rapid activation (Fig.1c).

84 A second control experiment targeted the non-essential surface antigen 1 gene (*sag1*)<sup>5</sup>.  
85 While >95% of parasites demonstrated loss of SAG1, we found that up to 50% of parasites  
86 also showed aberrant morphology of their nuclei in addition to loss of SAG1 (Fig.1d,e). This  
87 phenotype was only present in rapamycin-treated parasites co-expressing sCas9 and *sag1*  
88 sgRNA. No impact on parasite morphology was observed in RHsCas9 parasites (cultured  
89 with or without rapamycin), indicating that this phenotype is not caused by general toxicity of  
90 sCas9 (Fig.1e). To assess this phenotype further, we induced RHsCas9-*sag1* parasites for  
91 1h, mechanically released them from the host cell 48h later and allowed them to infect fresh  
92 HFF cells, thus representing the 2<sup>nd</sup> lytic cycle. Most of these parasites were negative for

93 SAG1 (79%  $\pm$ 4.8), and no aberrant morphology or nuclei were detectable, confirming that  
94 *sag1* is not critical for parasite survival *in vitro* (Fig.1e). Additional experiments were  
95 performed and demonstrated that the introduction of a double strand break (DSB) in the  
96 genome leads to a replication defect in a subpopulation of induced parasites (see  
97 Supplementary Text; Extended DataFig.2). Based on these results, we reasoned that the  
98 identification of specific defects in invasion, egress or other distinct phenotypes is straight  
99 forward, while genes involved in nuclear stability and/or replication can be identified by the  
100 significant increase in the percentage of parasites showing a defect in morphology and/or  
101 nuclear shape (Extended DataFig.2). Consequently, if the parasite population demonstrates  
102 a nuclear phenotype to less than 50% and parasites are still capable of invasion and egress,  
103 the corresponding candidate is likely not critical and clonal parasites can be isolated after the  
104 second lytic cycle, as shown for *sag1* (Fig.1d,e).

105 Furthermore, the use of specific indicator strains for parasite organelles and structures  
106 improves the readout of screens and allows identification of specific phenotypes  
107 (Supplementary Text).

108

109 *An indicator line for a screen of F-actin and egress mutants.*

110 To determine if this system could be used in phenotypic screens, we attempted to find  
111 candidates involved in the dynamics of F- actin with a special attention to the stabilisation  
112 and/or disassembly of the intravacuolar network (IVN) during egress. As previously  
113 described, actin and actin binding proteins significantly affect the dynamics of the IVN and  
114 therefore the synchronisation of parasite replication, segregation of the apicoplast and  
115 egress<sup>4</sup>.

116 To determine if candidates can be identified with high confidence in such a screen, we  
117 generated an indicator strain expressing the actin Chromobody CB-EmeraldFP (CbEm)<sup>4</sup> and  
118 the apicoplast marker FNR-RFP<sup>7</sup> (Fig.1f). Next, we assessed if disruption of previously  
119 described genes reproduces previously published phenotypes. At this end, we chose *sag1*,  
120 as negative control, dynamin related protein (*drpA*<sup>8</sup>), which should only affect apicoplast

121 division, actin-1 (*act1*<sup>4,9</sup>), actin depolymerisation factor (*adf*<sup>0</sup>) and *formin 2* (*frm2*)<sup>11</sup> (Fig.1g,h  
122 and Extended DataFig.1g), which should cause different effects on F-actin dynamics and  
123 apicoplast division. Since these previous studies demonstrated that depletion of proteins  
124 involved in F-actin dynamics (including ACT1) or apicoplast segregation did not result in  
125 abnormal morphology of nuclei, it is straight forward to exclude the non-specific phenotypes  
126 caused by a DSB.

127 Stable transfection with the respective sgRNA expression vectors and disruption of the target  
128 gene was validated by sequencing of the respective loci after gene disruption (Extended  
129 DataFig.1g). Parasitophorous vacuoles (PV) containing parasites with abnormal nuclei,  
130 representing the non-specific phenotype were quantified, but excluded from detailed analysis  
131 (Extended DataFig.2f). As expected, disruption of *sag1* or *drpA* had no detectable effect on  
132 the formation of the intravacuolar F-actin network (Fig.1h) and a strong defect in apicoplast  
133 segregation was observed in the case of *drpA*-disruption, as previously described<sup>8</sup>. In  
134 contrast, disruption of *act1* and *adf* led to disintegration and stabilisation of the intravacuolar  
135 network respectively (Fig.1h) as described<sup>4,9,12</sup>. In addition, disruption of the actin nucleator  
136 *frm2* also led to a more prominent staining of the intravacuolar network and abrogation of the  
137 cytosolic polymerisation close to the Golgi, replicating the effect observed when excising the  
138 locus using a DiCre strategy<sup>11</sup>. In all cases, apicoplast inheritance was affected as expected.  
139 Therefore, we concluded that the indicator strain allows the identification of specific  
140 phenotypes related to apicoplast maintenance, actin dynamics, or both.

141 We also assessed if delays in parasite egress can be identified to screen for genes required  
142 for host cell egress (Extended DataFig.3). In good agreement with the literature, disruption of  
143 *adf* and *act1* led to a significant delay in egress, while the behaviour of parasites with  
144 disrupted *sag1* was similar to WT parasites (Extended DataFig.3a,b,c).

145

146 *Phenotypic screening using a custom-designed sgRNA library.*

147 For the phenotypic screen, we curated a library containing genes without annotated signal  
148 peptides that are conserved only in apicomplexans, according to the annotation in the

149 ToxoDB 30 release, and have been hypothesised to be fitness conferring (phenotypic score  
150  $<-1.5$ )<sup>1</sup>. In addition, some genes were included that were of interest for independent projects,  
151 resulting in 320 candidates that were targeted (Supplementary Table2). As internal controls,  
152 sgRNAs targeting *gap40* (parasite replication<sup>6</sup>) and *profilin* (*prf*; F-actin dynamics and  
153 egress<sup>13</sup>) were included (Extended DataFig.4a,b) in the library. Synthesised sgRNAs were  
154 cloned into a vector containing the DHFR selection cassette as previously described<sup>14</sup>. The  
155 number of bacteria in the recovered sample carrying ligated plasmid was estimated to be  $3 \times$   
156  $10^6$  cfu, exceeding the number recommended to maintain complexity<sup>14</sup>. Library complexity  
157 was confirmed by sequencing sgRNA from 35 colonies picked at random (not shown), out of  
158 which we identified 29 unique gRNAs (83%).

159 Next, the library was transfected into the indicator strain, followed by drug selection, and  
160 sorting of single parasites into ten 96-well plates (Fig.2a).

161 We obtained 608 clonal parasites that were inoculated onto three replica plates. Two sets  
162 were induced with rapamycin for 48 and 72h, followed by fixation and automated imaging.  
163 Images were independently analysed twice by different authors and graded by the relative  
164 strength of phenotypes (Fig.2b). Using the decision tree shown in Fig.2b, we grouped  
165 phenotypes into “nuclear stability and replication” , “F-actin phenotype” and apicoplast  
166 segregation (Extended DataFig. 4c-h). It is important to mention that “nuclear stability and  
167 replication” phenotypes were selected based on the observed, significant increase of the  
168 ratios of PVs containing morphological aberrant parasites that are arrested in replication  
169 ( $>70\%$ ) compared to controls that show the non-specific nuclear phenotype ( $<50\%$ ).  
170 Therefore, screening for genes involved in replication and/or nuclear stability is still possible  
171 using sCas9 (see also Supplementary Text), as evidenced by the fact that we identified our  
172 internal control, *gap40* (for replication) and *prf* (for F-actin) multiple times (Supplementary  
173 Table3, Extended DataFig.4a,b).

174 We dismissed clones with integration of multiple different sgRNAs, which caused “super-  
175 aberrant” phenotypes (Extended DataTable3, Extended DataFig.4i). This procedure resulted  
176 in a total of 99 candidate genes (Supplementary Table3) that were prioritised by re-analysing



177 the obtained images. We focused on clones with the highest induction rates and excluded  
178 candidates with a strong replication defect (see above; Fig.2b). In summary, disruption of 42  
179 genes showed detectable differences in F-actin formation, apicoplast segregation and/or host  
180 cell egress (Extended Data Table 4). However, it should be noted that F-actin changes were  
181 relatively minor, when compared to the internal control (*prf*) (Extended Data Fig.4a) or the  
182 effects seen upon disruption of *adf* or *frm2* (Fig.1h).

183 We succeeded in tagging 12 of the 16 candidates classified as F-actin and/or apicoplast  
184 phenotype (Extended Data Fig.5; See Extended Data Fig.7a for tagging strategy).  
185 Interestingly, one of these genes, TGGT1\_208420, localised to the intravacuolar network and  
186 the apical pole of the parasite and was also found as important for natural egress (see below;  
187 Fig.3a and Extended Data Fig.6a).

188

#### 189 *Selection of candidates involved in parasite egress.*

190 Next, parasite egress was analysed 72h after inoculation and induction of sCas9. At this time  
191 point, most initially infected host cells were lysed and parasites reinvaded neighbouring host  
192 cells (Fig.2b). We identified 33 clones with a potential delay in host cell egress  
193 (Supplementary Table 4). Upon a second round of visual inspection, parasites forming  
194 smaller or aberrant PVs, indicating obvious replication defects, were excluded, resulting in  
195 the identification of candidates where conditional disruption resulted in a delayed egress  
196 phenotype (Supplementary Table 4).

197 Analysis of stimulated egress using calcium ionophore A23187 (Ci A23187) revealed that  
198 disruption of 4 candidate genes resulted in significantly delayed egress. In contrast, control  
199 parasites with disrupted *act1* and *adf*, were inhibited in egress (Extended Data Fig.3a and  
200 Fig.6a,b). Since disruption of the gene TGGT1\_252465, resulted in slower replication, it was  
201 excluded from additional analysis (Extended Data Fig.6c). Finally, the 3 remaining candidates  
202 also demonstrated a significant reduction in host cell invasion rates when compared to  
203 controls (Extended Data Fig.6d). One candidate (TGGT1\_248640) has recently been  
204 described as one of the non-discharge proteins, TgNd6<sup>15</sup>.

205 Here we focus our analysis on the remaining 2 candidates, TGGT1\_240380 and  
206 TGGT1\_208420, named conoid gliding protein (CGP) and signalling linker factor (SLF)  
207 respectively (Fig.2b).

208

### 209 *CGP and SLF are required for egress and invasion*

210 Database research did not reveal much information regarding the putative function of these  
211 hypothetical proteins. Both are highly conserved within the phylum apicomplexans and  
212 predicted to be critical for the parasite, based on their phenotypic scores<sup>16</sup>. SLF is predicted  
213 to be a putative sodium: neurotransmitter symporter with 12 transmembrane domains.  
214 Previously it was colocalised with other members of a Signalling Platform important for  
215 microneme secretion<sup>17</sup>. However, AID-based knockdown showed no phenotype, contrary to  
216 what we observed after Cas9-mediated disruption of *slf*. Regarding CGP, this protein is  
217 annotated in ToxoDB as a hypothetical protein and contains a CLU-central domain and a  
218 tetratricopeptide (TPR)-like domain. It is also predicted to localise at the plasma membrane  
219 based on hyperLOPID data<sup>18</sup>. However, no interaction partners nor potential function is  
220 predicted for this protein.

221 We tagged both genes C-terminally with Halo-Tag (*cgp*-Halo) or mCherry (*slf*-mCherry or *slf*-  
222 Halo) (Fig.3a, Extended DataFig.7a). Both proteins showed an apical localisation, as  
223 evidenced via colocalisation with the apical IMC-marker ISP1<sup>19</sup>. In addition, SLF also  
224 accumulated in the intravacuolar network that connects individual parasites within the PV<sup>4</sup>  
225 (Extended DataFig.8a).

226 To validate the phenotype seen with sCas9, genes were floxed in the RHDiCre $\Delta$ *Ku80* strain<sup>20</sup>  
227 (Fig.3b; Extended DataFig.7, Fig.8a and Fig.9a) to generate conditional null mutants (cKO).  
228 Induction of DiCre using rapamycin led to a severe growth defect, as evidenced by plaque  
229 assays, confirming their critical role during the asexual life cycle of the parasite (Fig.3c).  
230 Further analysis fully confirmed the phenotype obtained using sCas9 and demonstrated a  
231 crucial function of both proteins in host cell egress and invasion, while parasite replication,

232 morphology, apicoplast and secretory organelles were not affected (Fig.3d,e; Extended  
233 DataFig.8 and Fig.9).

234 Gliding motility was significantly reduced in both mutants (Fig.3f; Extended DataFig.8e,  
235 Fig.9c; Movie\_S1). Interestingly, in the case of parasites lacking *slf* (*slf*-cKO) gliding motility  
236 and egress (Fig.3e,f; Extended DataFig.8e,f) could be partially rescued upon addition of Ci  
237 A23187 (Extended DataFig.8f; Movie\_S2), indicating that it is involved in a signalling  
238 cascade, upstream of intracellular calcium release. Indeed, *slf*-cKO showed a significantly  
239 reduced secretion of micronemes, that was less severe when Ci A23187 was used as an  
240 inducer, compared to BIPPO<sup>21</sup> (54.5% versus 74.3% microneme secretion reduction; Fig.3g;  
241 Extended DataFig.8). Therefore, the phenotype of *slf*-cKO appeared similar to the  
242 phenotypes observed upon deletion of components of the phosphatidic acid (PA) signalling  
243 platform, such as diacylglycerol kinase 2 (DGK2), cell division control 50 related protein  
244 (CDC50.1), guanylate cyclase (GC) or unique GC organiser (UGO)<sup>17</sup>.

245 In the case of *cgp* knockout parasites (*cgp*-cKO), egress was blocked irrespective of addition  
246 of Ci A23187, BIPPO or Propanolol (Fig.3e). Furthermore, no defects of microneme  
247 secretion could be observed (Fig.3h; Extended DataFig.9), placing this protein into a different  
248 functional category.

249

250 *CGP and SLF act at two distinct, temporally controlled steps.*

251 We then characterised the sequential action of CGP and SLF during host cell egress. The  
252 intravacuolar network is rapidly disintegrated early in the egress process<sup>4</sup>, thereby acting as  
253 an early indicator for initiation of host cell egress. Therefore, we introduced CbEm<sup>4</sup> into the  
254 UPRT locus of both mutants to analyse localisation and dynamics of F-actin (Fig.4a;  
255 Extended DataFig.7k,l; Movies\_S3, S4 and S5).

256 When analysing F-actin dynamics upon induction of egress, the following steps can be  
257 differentiated in WT parasites: 1) initiation of intravacuolar network disassembly, 2) reduction  
258 of F-actin nucleation close to the Golgi, probably caused by FRM2<sup>4</sup> and 3) strong posterior  
259 accumulation of F-actin and activation of motility (Fig.4a,b). In the case of *slf*-cKO parasites,

260 none of these steps could be observed indicating that initiation of egress is completely  
261 blocked and that the initial signals leading to the induction of microneme secretion are  
262 identical with regulation of F-actin dynamics during host cell egress (Fig.4a,b). This  
263 phenotype was partially rescued upon addition of Ci A23187 (Extended Data Fig.8 and  
264 Fig.10a,b). Interestingly, parasites which did not egress after induction with Ci A23187 were  
265 still able to efficiently disassemble the IVN in most cases, and F-actin accumulation at the  
266 posterior pole was initiated. Despite this, motility was not initiated at the time of fixation or  
267 after 10 mins of recording. (Movie\_S3. Extended DataFig.8).

268 Intriguingly, induction with propranolol led to a different egress phenotype, when compared to  
269 induction with BIPPO. Here the parasites that remained within the PVM were able to  
270 disassemble the filaments but appeared unable to initiate motility (Fig.4a; Movie\_S3).  
271 Furthermore, these parasites changed their shape and appeared rounded up, which was  
272 only observed upon induction of *sif*-cKO parasites with propranolol.

273 In contrast, deletion of *cgp* led to a block in a later stage during egress. While disassembly of  
274 the intravacuolar network and reduction of F-actin nucleation close to the Golgi occurred  
275 normally, neither posterior accumulation of F-actin nor parasite motility appears to be  
276 initiated (Fig.4a,b; Movie\_S4).

277 In summary, this analysis highlights that SLF and CGP act at two temporally different steps  
278 during host cell egress. While SLF acts at the initiation step, CGP acts downstream, after the  
279 intravacuolar F-actin network has been disassembled.

280 Finally, we were interested to know if the PV-membrane (PVM) is dissolved. Therefore, we  
281 expressed *sag1*ΔGPI-dsRed, which is secreted into the PV. Upon lysis of the PV this protein  
282 diffuses into the cytoplasm of the host cell, as seen in case of control parasites (Fig.4c, top  
283 row). Deletion of CGP had no influence on lysis of the PV, since dsRed signal diffused at a  
284 similar time as seen in case of controls. In contrast, upon deletion of SLF, the PVM remained  
285 intact and dsRed signal is trapped within the PV (Fig.4c; Movie\_S5).

286

287

288 *SLF is required for integrity of the PA signalling complex*

289 Bioinformatic predictions of SLF place this protein into the family of sodium neurotransmitter  
290 symporters and demonstrates that it is highly conserved in all apicomplexan parasites.

291 This protein was previously identified as a putative and dispensable interaction partner of the  
292 signalling platform, since knockdown using the auxin-inducible degron (AID) system had no  
293 effect on the parasite lytic cycle<sup>17</sup>. However, disruption and excision of *slf* demonstrated one  
294 of the strongest phenotypes obtained in this screen, suggesting that the AID system is  
295 insufficient to knockdown protein levels of SLF. Indeed, SLF colocalised with other members  
296 of the PA signalling pathway such as GC, CDC50.1 and UGO (Fig.5a) at the apical tip of the  
297 parasite and the intravacuolar network. Importantly, deletion of SLF results in mislocalisation  
298 of other components of this signalling complex and vice versa (Fig.5b,c), indicating that this  
299 complex is assembled early in the secretory pathway, probably the ER, and only reaches its  
300 final destination if all partners are present. This was seen in 100% of vacuoles, where one  
301 component is missing. While this confirms an important structural role of SLF for functional  
302 assembly of the signalling complex, future studies are required to determine if this protein  
303 also acts as a sodium neurotransmitter as predicted in ToxoDB. In a first attempt, we focused  
304 on GABA ( $\gamma$ -aminobutyric acid) as a potential substrate for this putative symporter, since it  
305 was demonstrated that *T. gondii* synthesises high levels of GABA<sup>22</sup> and modulates host cell  
306 migration using GABA as messenger<sup>23</sup>. However, we were unable to either complement the  
307 phenotype by adding increasing concentrations of GABA or to mimic the phenotype by  
308 addition of GABA analogues (Extended DataFig.10c,d). In conclusion, SLF is a critical  
309 component for the integrity of the PA signalling platform required for egress. Future analysis  
310 will reveal if this protein is directly involved in the signalling cascade by acting as a  
311 symporter.

312

313 *CGP is a novel component of the conoid.*

314 STED imaging showed a localisation of CGP anterior to the conoid markers RNG2, which  
315 localises to the second apical polar ring, and SAS6-like (SAS6L), a marker of the conoid

316 body<sup>24</sup>. This apical localisation was detected in retracted and protruded conoids (Fig.6a).  
317 Importantly, conoid structure appeared unaffected upon deletion of *cgp* (Fig.6b) indicating  
318 that this protein does not play a key role for the integrity of the conoid itself. Similarly, the  
319 secretory organelles (micronemes and rhoptries) were not affected by deletion of *cgp* and  
320 secretion of micronemes occurred normally (Fig.3h; Extended DataFig.9e,f).  
321 While bioinformatic analysis of this protein suggests that it is highly conserved within  
322 apicomplexan parasites (not shown), no clear orthologue could be identified in other  
323 eukaryotes. Therefore, future studies are required to identify potential interaction partners  
324 and the mechanistic action during host cell egress. Moreover, it would be interesting to  
325 determine if their function is also conserved in other apicomplexan parasites.

326

## 327 **Discussion**

328 In this study, we adapted an efficient and tightly regulated conditional Cas9-system based on  
329 sCas9<sup>3</sup>. Our detailed analysis of this system demonstrated that repair of DSB introduced by  
330 Cas9 is occasionally inefficient, leading to aberrant, non-specific phenotypes in a  
331 subpopulation of parasites. While these effects need to be considered when conducting a  
332 phenotypic screen, they can easily be deduced from the readout of the screen, especially  
333 when modern, automated image analysis methods are used that are now also available to  
334 determine the phenotype of *Toxoplasma*-Host interactions<sup>25</sup>. Computational image analysis  
335 tools should allow to not only exclude but to differentiate between the non-specific nuclear  
336 and specific replication phenotypes. In order to do so, a huge dataset of known phenotypes  
337 needs to be created in order to train the algorithms<sup>26</sup>, an effort well worthwhile to undertake,  
338 especially when larger genome-wide screens for multiple phenotypes are planned.

339 Here, screening of an indicator strain that co-expresses fluorescent actin binding  
340 chromobodies (CbEm)<sup>4</sup> and an apicoplast marker<sup>7</sup> allowed the identification of mutants with  
341 defects in apicoplast maintenance and F-actin dynamics in addition to mutants with inhibited  
342 host cell egress. Therefore, we curated a sgRNA library targeting 320 candidate genes that  
343 are conserved among apicomplexans. Based on the phenotypic characterisation of identified

344 mutants, we did not identify a novel factor that is directly involved in regulation and  
345 organisation of F-actin dynamics during intracellular replication. Instead, several factors were  
346 identified, where F-actin dynamics was only slightly altered, when compared to positive  
347 controls (Prf, ADF, ACT1). In contrast, two novel genes identified here, *slf* and *cgp*, are  
348 crucially involved in the regulation of actin dynamics during host cell egress where they play  
349 distinct roles.

350 Time-lapse microscopy analysis suggests that disassembly of the intravacuolar network  
351 precedes the initiation of motility and egress of parasites from the PV<sup>4</sup> (Fig4a; Movie\_S3,  
352 S4). Indeed, stabilisation of F-actin by depletion of ADF results in an egress phenotype,  
353 where parasites were able to initiate motility, but remain connected by the intravacuolar  
354 network (Fig.6c, Extended DataFig.3).

355 When we applied this analysis to conditional mutants for SLF and CGP, we observed  
356 important differences in the behaviour during host cell egress. While deletion of SLF caused  
357 an early block in host cell egress, where neither the intravacuolar network nor the PVM is  
358 disassembled, deletion of CGP caused a late block in egress, where parasites disassembled  
359 both the intracellular F-actin network and PVM but are incapable of initiating motility and  
360 leaving the host cell. While CGP is not involved in microneme secretion, it is likely that it  
361 directly or indirectly regulates gliding motility by regulating F-actin dynamics, since deletion of  
362 CGP resulted in clear differences in F-actin dynamics, as evidenced by missing posterior  
363 accumulation of F-actin.

364 In the case of SLF, we found that this protein is an important component of a previously  
365 described PA signalling platform required for host cell egress<sup>17</sup>, since deletion of SLF  
366 resulted in mislocalisation of the remaining components, CDC50.1, GC or UGO within the ER  
367 of the parasite. Together this indicates that the signalling complex might need to be  
368 assembled within the ER before being transported to the apical tip and intravacuolar network,  
369 where it fulfils its critical function.

370 These findings highlight the robustness of this approach for finding essential genes based on  
371 their function. In future screens, establishment of different indicator lines expressing markers

372 for the secretory organelles, IMC or mitochondria could be used to specifically identify genes  
373 involved in organellar biogenesis, parasite replication or maintenance of the endosymbiotic  
374 organelles, to name a few examples for future applications of this technology  
375 (Supplementary Text and Extended DataFig.10e,f,g).

376 Concurrently with our work, Smith and colleagues developed an alternative strategy, based  
377 on high-throughput CRISPR-mediated tagging of candidate genes with the AID-system and  
378 demonstrate the efficiency of their strategy by labelling and downregulation of the *T. gondii*  
379 kinome, resulting in the characterisation of kinases, involved in diverse functions. As with all  
380 technologies, both approaches have their advantages and disadvantages. While the mAID-  
381 based screening approach allows direct localisation and rapid regulation of the protein of  
382 interest, there is a potential risk for incomplete protein knock-down, the difficulty to  
383 functionally tag some proteins, and limitation to proteins that are accessible to the  
384 degradation machinery. The sCas9-based screen on the other hand acts directly on the  
385 DNA-level by introduction of indel mutations in the gene of interest. The kinetics of protein  
386 depletion is probably comparable to the Tet-inducible and DiCre-system<sup>27</sup> and significantly  
387 slower compared to AID. Therefore, screens based on sCas9 have no restriction regarding  
388 the gene of interests and can in principle be performed with all gRNAs-libraries designed  
389 previously for other projects. Indeed, we are currently performing a genome wide screen  
390 using sCas9 (Jimenez-Ruiz et al., in preparation). A drawback of sCas9 (as with all cas9-  
391 based approaches that rely on NHEJ repair of the introduced DSB) is the occurrence of  
392 aberrant, nuclear phenotypes in a subpopulation of parasites, making it somewhat difficult to  
393 clearly interpret nuclear and replication phenotypes without further downstream analysis (see  
394 also Supplementary Text for more details). In conclusion, both strategies are highly  
395 complementary and have a huge potential to screen the *T. gondii* genome in search for key  
396 candidates based on their function and resulting phenotypes.

397

## 398 **Materials and Methods**

### 399 *Cloning DNA constructs*



400 The N- and C-termini of the Cas9 enzyme (split4 variant) were amplified from the original  
401 plasmids provided by Zetsche and colleagues<sup>3</sup> via PCR. The PCR amplicons were ligated  
402 into the pGEM®-T Easy vector and sequenced. Subsequently, they were cloned into the  
403 *Toxoplasma* expression vector p5RT70-HX<sup>28</sup> via the restriction enzymes EcoRI (NEB;  
404 R0101S) and PacI (NEB; R0547S). For the C-term-Cas9 vector, the *hx* selection marker was  
405 removed by restriction with SacII (NEB: R0157S). The resulting plasmids were confirmed by  
406 sequencing.

407 pU6-*sag1* gRNA-scaffold and pU6-*gap40* gRNA-scaffold sequence was synthesised and  
408 cloned into a backbone vector containing the DHFR resistance cassette by GeneScript. The  
409 Q5® Site-Directed Mutagenesis Kit (New England Biolabs) was used to insert sgRNAs  
410 targeting control genes of interest (*act1*, *adf*, *frm2* and *drpA*) into the synthesised sgRNA  
411 plasmid according to the manufacturer's instructions. Importantly, a universal reverse primer  
412 was used together with a forward primer to which the whole sgRNA sequenced was  
413 attached, see also<sup>29</sup>. Further sgRNAs used in this study were cloned into the universal pU6  
414 vector via BsaI digestion, primers annealing and standard ligation using T4 Ligase (see oligo  
415 sequences Supplementary Table 5) as previously described<sup>29</sup>. All sgRNA-plasmids were  
416 confirmed by sequencing.

417 To generate mutated *sag1*\*, genomic DNA was amplified and inserted via EcoRI and PacI  
418 into p5RT70-HX<sup>28</sup>. Mutations at the sgRNA binding sequence were introduced via  
419 mutagenesis using Q5 Site Mutagenesis following manufacturer's protocol (NEB; E0554S)  
420 using primers described in Supplementary Table 5.

421

#### 422 *Culturing of T. gondii and host cells*

423 *T. gondii* tachyzoites were passaged onto Human foreskin fibroblasts (HFFs; ATCC, SCRC-  
424 1041) monolayers at 37 °C and 5% CO<sub>2</sub> in DMEM (Sigma, D6546) supplemented with 10%  
425 FBS (BioSell FBS.US.0500), 4mM L-Glutamate (Sigma, G7513) and 20 µg/ml gentamicin  
426 (Sigma G1397).

427

428 *Generation of transgenic parasites*

429 Freshly lysed *Toxoplasma* tachyzoites were transfected with Amaxa 4D-Nucleofector system  
430 (Lonza; AAF-1003X).  $\sim 1 \times 10^6$  parasites were centrifuged and resuspended in 50  $\mu$ l P3 buffer.  
431 Up to 20  $\mu$ g of DNA for transfection, including vectors, donor DNA and/or single stranded  
432 DNA, was ethanol precipitated and resuspended in another 50  $\mu$ l of P3 Buffer. Both  
433 resuspensions were mixed in a 100  $\mu$ l cuvette (P3 Primary cells 4D-Nucleofector X kit L,  
434 V4XP-3024, Lonza). The programme FI-158 was used for electroporation. Immediately after  
435 transfection, parasites were resuspended in fresh complete DMEM and added onto a dish  
436 with confluent HFF cells.

437 For generation of sCas9-parasites, a total of 20  $\mu$ g of the vectors containing the sCas9  
438 subunits were linearised with NotI (NEB; R3189S) and transfected simultaneously in  
439 RH $\Delta$ *hxgprt* (RH $\Delta$ HX), adding NotI restriction enzyme to the transfection mix. Integrants were  
440 selected with 25 mg/ml mycophenolic acid (MPA; Sigma; M3536) and 40 mg/ml of xanthine  
441 (Sigma; X3627)<sup>30</sup>. After isolating a clone containing both functional subunits, sgRNAs against  
442 the *hxgprt* cassette were transfected and the parasites were selected with 80 mg/ml 6-  
443 Thioxanthine (Sigma-Aldrich; 852570)<sup>30</sup>. The *hxgprt* cassette was then sequenced to confirm  
444 the introduction of indels.

445 Vectors containing sgRNAs targeting control genes (*gap40*, *sag1*, *act1*, etc) were linearised  
446 via NotI and transfected into RH $\Delta$ HXsCas9 as described above. To select for the *dhfr*  
447 resistance marker, parasites were treated with 1  $\mu$ M pyrimethamine (Sigma 46706; Donald  
448 and Roos 1993). Insertion of sgRNAs were confirmed by PCR of the sgRNA cassette  
449 (Extended DataFig.1f).

450 For the generation of RHsCas9-CbEm-FNR-RFP, RHsCas9 parasites were first transfected  
451 with the vector containing the CbEm cassette<sup>4</sup>. Transfectants were enriched via  
452 Fluorescence Assisted Cell Sorting (FACS; S3 BioRad), and a clone was isolated via limiting  
453 dilution. Secondly, the vector containing FNR-RFP was linearised via NotI and transfected  
454 into RHsCas9-CbEm strain and selected with 20  $\mu$ g/ml chloramphenicol<sup>5</sup>. After selection,  
455 clones were isolated by limiting dilution.

456

457 *sgRNA library generation and transfection*

458 A list of guide RNAs was obtained after searching in ToxoDB (release 30. February 2017) for  
459 genes annotated as apicomplexan specific, without signal peptide and with a phenotypic  
460 score  $\leq -1.5$ . Control genes, such as *gap40* and *prf*, were included to this list. 1 gRNA per  
461 gene was selected from Sidik et al. (2016) genome wide library (Supplementary Table 2).

462 The resulting 320 gRNAs were synthesised (CustomArray, Inc. USA), amplified by PCR, and  
463 cloned as a pool into a plasmid using Gibson Assembly (NEB E26115) as performed by Sidik  
464 et al. (2018)<sup>14</sup>. The vector plasmid carries a pU6 promoter, and a DHFR cassette. Assembled  
465 plasmids were transformed in two batches, and bacteria allowed to grow to log phase. The  
466 plasmids were extracted, purified, pooled, and 200 ng retransformed into the bacteria for  
467 further library amplification. Library complexity was estimated based on 1) the number of  
468 independent colonies obtained after transforming bacteria with 200 ng of library DNA (as  
469 described in Sidik et al. 2018<sup>14</sup>) and 2) random isolation of individual colonies and  
470 sequencing of the respective sgRNA. From the colony picking, 10  $\mu$ g of different isolated  
471 gRNAs were transfected individually into RHsCas9-CbEm-FNR-RFP and analysed in parallel  
472 to the screen described below.

473 Following the generation of the vector library, 60  $\mu$ g of pooled plasmid library was transfected  
474 into RHsCas9-CbEm-FNR-RFP line specifically created to be used as an indicator strain for  
475 this project. This transfection gave rise to a pool of parasites which were collectively carrying  
476 the guide RNA library. A minimum of  $1 \times 10^7$  parasites were passaged each time. To obtain  
477 clonal populations, transfectants were subjected to 3 weeks of pyrimethamine selection  
478 followed by FACS (BD FACSAriaIII) into ten 96-well plates, one event per well.

479

480 *Phenotypic screening of sCas9 mutants*

481 Conditional mutagenesis via sCas9, was induced using 50 nM rapamycin (Sigma; R0395-  
482 1MG) for 48 and 72 h, and the plates were imaged using the LasX navigator on a Leica DMI8  
483 widefield microscope attached to a Leica DFC9000 GTC camera, using a 20x objective. After

484 choosing the correct carrier on the navigator, the plates were aligned and three random  
485 images were taken from each well, using the 'On demand' adaptive autofocus setting. The  
486 images obtained were independently screened by eye by two investigators before  
487 subsequent selection of the candidate clones. Clones which were seen to exhibit aberrant  
488 organellar morphologies or altered F-actin dynamics, and egress defects were then selected  
489 and the guide RNAs present in the clonal populations, which exhibited phenotypes deemed  
490 relevant to the project, were then sequenced to identify the gene disrupted. To prioritise the  
491 candidates for further characterisation, the phenotypes observed were graded from 1 (least  
492 severe) to 4 (most severe) (Supplementary Table 3).

493

#### 494 *Generation of tagged and floxed strains*

495 Guide RNAs for cleavage upstream and downstream of the genes of interest were designed  
496 using EuPaGDT<sup>31</sup>. Sequences of all sgRNAs employed in this study are detailed in  
497 Supplementary Table 1. The sgRNAs were ligated into a vector coding for Cas9-YFP  
498 expression, as has been previously described<sup>32</sup>.

499 Repair templates for integration of a loxP sequence and a tag were generated as in Stortz et  
500 al. (2019)<sup>11</sup>. Briefly, repair templates carrying the upstream loxP sequence were ordered as  
501 ssDNA oligos (ThermoFischer Scientific), the loxP sequences being flanked by 33 bp of  
502 homology. The repair templates carrying tags, such as 3xHA, SYFP2, Halo and SNAP, were  
503 generated by PCR, where the 50 bp of homology flanking the tags were introduced via the  
504 primer. The repair templates were pooled according to the gene and purified using a PCR  
505 purification kit (Blirt; EM26.1) (Extended DataFig.7a,b).

506 Parasite transfection, sorting and screening for positive mutants was done according to  
507 Stortz *et al.* (2019)<sup>11</sup>. Briefly, newly released RHDiCre $\Delta ku80$  tachyzoites<sup>33</sup> were transfected  
508 with the repair templates and 10-12  $\mu$ g of vectors (encoding Cas-YFP and the respective  
509 sgRNAs) as described above. The parasites were mechanically egressed 24 to 48 h after  
510 transfection, passed through a 3  $\mu$ m filter, and those transiently expressing Cas9-YFP  
511 enriched via FACS (FACSARIA III, BD Biosciences) into 96-well plates (a minimum of 3

512 events per well). Resultant clonal lines were screened by PCR and repair template  
513 integration confirmed by sequencing (Eurofins Genomics).

514 For the insertion of CbEm into tagged lines, a specific sgRNA targeting the uracil  
515 phosphoribosyltransferase (UPRT) locus was designed and cloned into a Cas9-  
516 YFP-expressing vector. CbEm cassette from the original plasmid used in Periz *et al.*<sup>4</sup>, was  
517 PCR amplified and integrated into the UPRT locus (Extended DataFig.7k).

518

#### 519 *Immunofluorescence assays*

520 Parasites were fixed in 4% paraformaldehyde for 15-20 minutes at room temperature.

521 Samples were blocked and permeabilised in phosphate-buffered saline (PBS) with 2% BSA  
522 and 0.2% Triton X-100 for at least 20 minutes. Antibody labelling was performed using the  
523 indicated combinations of primary antibodies for 1 h, followed by the incubation with

524 secondary antibodies for another 45 min. All antibodies are listed in Supplementary Table 6.

525  $\alpha$ -GFP-ATTO 488 (1:500, Nano Tag Biotechnologies, N0304-At488-L) was directly used for  
526 1h after permeabilisation. Parasites containing Halo or SNAP tags were incubated with

527 specific dyes for 1 h and washed away, followed by incubation with media for 1 h before

528 fixation unless specifically indicated elsewhere (see Supplementary Table 6). Images were

529 taken using Leica DMI8 Widefield microscope or an Abberior 3D STED microscope. The

530 library parasite pictures obtained using the Abberior 3D STED microscope were taken using

531 the confocal setting for FNR-RFP and Hoechst, and STED for the CbEm imaging.

532

#### 533 *Invasion/replication assays*

534 24 h invasion/replication assays were performed using sCas9 parasite clones isolated as  
535 previously described, with some changes<sup>34</sup>.  $5 \times 10^6$  parasites were used to infect covers and

536 were left to settle down on ice before allowed invasion for 20 min. Parasites were stained

537 with  $\alpha$ -SAG1 antibody without permeabilisation and  $\alpha$ -GAP45 antibody after permeabilisation.

538 For invasion, the number of vacuoles in 10 randomly selected fields of view were counted for

539 each parasite line and condition. For replication, the number of parasites per vacuoles were  
540 counted. At least 100 vacuoles were counted.

541 In the case of RHDiCre $\Delta ku80$  floxed strains, loxPcgp-Halo parasites were used for  
542 invasion/replication assays, loxPs/f-Halo were used for invasion assays, and loxPs/f-mCherry  
543 were used for replication assays. Parasites were pre-induced for 96 h  $\pm$  50 nM rapamycin.  
544 Parasites were then mechanically egressed, and  $5 \times 10^6$  parasites (for invasion assays) or  
545  $4 \times 10^6$  (for replication assays) were inoculated in each well and left to invade for 1 h.

546 For invasion assays, parasites were allowed to settle on ice for 10 min, and then allowed to  
547 invade for 1 h at 37 °C before fixation. Subsequent IFAs were done following the same  
548 protocol as the invasion assays done on the sCas9 parasite strains. A minimum of 150  
549 parasites were counted to calculate the percentage of invaded parasites.

550 For replication assays, samples were washed 3 times with DMEM to remove non-attached  
551 parasites and left at 37 °C for another 24 h. Samples were fixed with 4% PFA and labelled  
552 with  $\alpha$ -GAP45 (loxPcgp-Halo) or IMC1 and  $\alpha$ -RFP (loxPs/f-mCherry).

553 LoxPcgp-Halo parasites were pre-incubated with HaloTag Oregon Green dye (0.2  $\mu$ M) for 1  
554 h, whereas loxPs/f-Halo parasites were incubated with Halo Janelia 646 (20 nM) for 15 h  
555 prior to the start of the invasion assay.

556 These experiments were carried out in triplicate and a minimum of 100 parasites/ vacuoles  
557 were counted ( $n = >100$ ). In case of rapamycin induced floxed parasites (cKO), only  
558 parasites/ vacuoles lacking signal for SLF or CGP were included in the counting.

559

#### 560 *Plaque assay*

561 A total of 500-1000 parasites per well were inoculated into confluent HFFs in 6 well-plates  
562 and incubated for 6 days  $\pm$  50 nM rapamycin<sup>34</sup>.

563 In case of GABA (Tocris, 0344) or Gabapentin (Sigma-Aldrich, G154) plaque assays, media  
564 was supplemented with different concentrations of GABA (100 mM stock concentration) or  
565 Gabapentin (50 mM stock concentration).

566 Images were taken using the LAS X Navigator software and a Leica DMI8 Widefield  
567 microscope using 10× objective (Microsystems). Starting in the middle of the well, an area of  
568 12 x 12 fields was imaged. Focus maps were created and autofocus controls were applied  
569 for taking the final images. After acquisition of the images, “mosaic merge” processing tool in  
570 LAS X software was used for merging the pictures into one big final image.

571

### 572 *Egress assays*

573 For egress assays depicted in Extended DataFig. 3, induced (50 nM Rapamycin) and non-  
574 induced RHsCas9-CbEm-*adf/sag1* parasites were grown for 48 h. Egress was then induced  
575 by incubating parasites with 2 μM Ci A23187 for 8min under normal culturing conditions.  
576 Subsequently, parasites were fixed with 4% PFA for 20min and α-SAG1 or α-GAP45 were  
577 used for parasite visualisation.

578  $1 \times 10^5$  sCas9 background parasites were grown on HFF cells incubated with  $\pm$  50 nM  
579 rapamycin for 4 h. They were then washed with DMEM three times to remove rapamycin and  
580 any extracellular parasites. Parasites were maintained for another 44 h in the incubator at 37  
581 °C before inducing egress.

582 In case of parasites floxed in the DiCre strain, parasites were pre-treated  $\pm$  50 nM rapamycin  
583 for 24 h and  $3 \times 10^5$  were inoculated onto confluent HFF cells, incubated for 1 h at 37 °C,  
584 then washed 3 times with PBS and maintained at 37 °C for 32 h before inducing egress. Halo  
585 tagged parasites were pre-incubated with HaloTag Oregon Green (0.2 μM) or Janelia Fluor  
586 646 (20 nM) for 1 h and washed three times with PBS before inducing egress. To induce  
587 parasite egress, media was exchanged with pre-warmed DMEM without serum but  
588 supplemented with various inducers for different lengths of time (2 μM Ci A23187 (Sigma-  
589 Aldrich, C7522-1mg) for 5 min, 50 μM BIPPO (a phosphodiesterase inhibitor that stimulates  
590 microneme secretion<sup>21</sup>; Thompson Lab) for 5 min, or 125 μM Propranolol hydrochloride  
591 (Merck, 40543) for 7 min).

592 After induction, sCas9 expressing parasites were fixed with 4% PFA and the number of  
593 egressed and non-egressed vacuoles counted. DiCre-expressing parasites were fixed with

594 either 4% PFA or 100% methanol.  $\alpha$ -SAG1 or  $\alpha$ -GAP45 antibodies were used for the  
595 visualisation of parasites. In case of rapamycin induced floxed parasites, only vacuoles  
596 lacking signal of the respective protein was considered in the counting (cKO). At least 100  
597 vacuoles were counted for each condition and replicate and the percentage of the egressed  
598 vacuoles was calculated.

599 For time-lapse images, floxed parasites expressing CbEm (*loxPcgp-Halo/CbEm* and *loxPslf-*  
600 *Halo/CbEm*) were treated  $\pm$  50 nM rapamycin for 24 h and then mechanically released and  
601 inoculated onto glass-bottom live cell dishes, and cultured for a minimum of 32 h before  
602 inducing egress. Halo-tagged parasites were pre-incubated with Janelia Fluor 646 (20 nM)  
603 for around 5 h followed by washing 3 times with PBS and then incubated with normal media  
604 for at least 1 h before egress induction.

605 Dishes were placed in the pre-warmed chamber of Leica DMI8 microscope and media was  
606 exchanged with complete Fluorobrite DMEM (ThermoFischer Scientific, A1896701)  
607 containing the respective inducers. Videos were taken with a 63x oil objective at 0.33 frames  
608 per second (FPS). Videos were recorded in triplicate per condition as a minimum. In case of  
609 conditional knockouts, only vacuoles lacking the signal for SLF or CGP were recorded (cKO).  
610 For calculating the dynamics of CbEm after stimulating egress chemically, regions of interest  
611 (ROI) were drawn around the apicoplast region, the region between basal CbEm labelling  
612 and the apicoplast (termed nuclear region), the *T. gondii* cell, and a background region  
613 outside the vacuole. Relative intensity of the CbEm in apicoplast region was then determined  
614 as:

$$relative\ intensity = \frac{(mean\ apicoplast - mean\ nuclear\ region) \times apicoplast\ area}{(mean\ total\ Toxoplasma - mean\ background) \times total\ toxoplasma\ area}$$

615

616 Relative intensity of the CbEm in basal pole region was then determined as:

617

$$relative\ intensity = \frac{(mean\ basal\ part - mean\ nuclear\ region) \times basal\ part}{(mean\ total\ Toxoplasma - mean\ background) \times total\ toxoplasma\ area}$$

618

619 where mean was defined as:



$$Mean = \frac{RawIntDen}{area}$$

620

621 To check PVM integrity, loxP*cgp*-Halo/CbEm and loxP*s/f*-Halo/CbEm were treated with  $\pm$  50  
622 nM rapamycin for 24 h and transfected with the vector pTub- *sag1* $\Delta$ GPI-dsRed. 48 hours  
623 later, egress was induced with 50  $\mu$ M BIPPO and recorded as described above. Over 10  
624 egress events were recorded for each condition.

625 To check the F-actin IVN network upon induction of egress with Ci A23187, assays were  
626 performed as described above for loxP*s/f*-Halo/CbEm strain infecting HFF on coverslips with  
627  $2.5 \times 10^5$  parasites. After induction with 2  $\mu$ M A23187 for 5 min, parasites were fixed with  
628 cytoskeleton buffer (CBs)<sup>35</sup> for 25 min and followed by 50 mM NH<sub>4</sub>CL for 10 min. Anti-GFP  
629 Atto-488 antibody was used to amplify the CbEm signal. CB buffer was previously reported in  
630 Periz et al. (2019) and is the result of a mixture of CB1 and CB2 (4:1). CB1: MES pH 6.1 10  
631 mM, KCL 138 mM, MgCl<sub>2</sub> 3 mM, EGTA 2 mM, 5% PFA. CB2 :MES pH6.1 10 mM, KCL  
632 163.53 mM, MgCl 3.555 mM, EGTA 2.37 mM, Sucrose 292 mM.

633

#### 634 *Trail deposition assay and live gliding assay*

635 For trail deposition assays, induced (50 nM rapamycin, 72 h for loxP*cgp*-Halo and 96 h for  
636 loxP*s/f*-mCherry) and non-induced (72 h for loxP*cgp*-Halo and 96 h for loxP*s/f*-mCherry)  
637 parasites were washed, mechanically egressed via 26-gauge needles and filtered through 3  
638  $\mu$ m filters. Parasites were then centrifuged at 1000 x g for 5 min at room temperature and the  
639 pellet was resuspended in pre-warmed endo buffer (44.7 mM K<sub>2</sub>SO<sub>4</sub>, 10 mM MgSO<sub>4</sub>, 100  
640 mM sucrose, 5 mM glucose, 20 mM Tris, 0.35% w/v BSA, pH 8.2) at a concentration of  
641  $2 \times 10^6$  parasites/ml. 1 ml of this mixture was added to a FCS coated glass-bottom live cell  
642 dish and incubated for 15 min at room temperature. Endo buffer was gently replaced with  
643 1ml of pre-warmed sterile gliding buffer (1mM EGTA and 100mM HEPES in HBSS solution).  
644 Parasites were incubated for 20 min at 37 °C and then fixed with 4% PFA for 20 min.  
645 Parasites were stained with  $\alpha$ -*Toxoplasma gondii* antibody (Abcam; see Supplementary

646 Table 6) without permeabilisation. 15 random fields of view were imaged and the total  
647 number of trails parasites left were counted.

648 For live gliding assays, to measure parasite gliding kinetics, time-lapse videos were taken  
649 with a 63x objective at 2 FPS using a Leica DMI8 microscope using DIC. After 20 minutes of  
650 recording per condition, a Z-stack image of the fluorescence channel targeting the protein of  
651 interest was taken to distinguish the cKO from the non-induced parasites. Only cKO were  
652 considered for the analysis for rapamycin induced parasites. Halo tagged parasites were pre-  
653 incubated with Janelia Fluro 646 dye (20 nM) or HaloTag TMR (500 nM) at least 2 hours as  
654 described above before performing live gliding assays. Parasite motility was analysed by  
655 manual tracking plugin tool by Icy software. All the assays were done in  $\text{Ca}^{2+}$ -free gliding  
656 buffer unless otherwise indicated.

657 For trail deposition and gliding assays with 2  $\mu\text{M}$  Ci A23187, compounds were added to the  
658 gliding buffer described above.

659

#### 660 *Microneme secretion assay*

661 Microneme secretion assay protocol was adapted from Bisio *et al.* (2019)<sup>17</sup>. Parasites treated  
662 for 72 h  $\pm$  50 nM rapamycin were mechanically released by 26-gauge needles and washed  
663 twice with cold intracellular buffer and then being resuspended in pre-warmed intracellular  
664 buffer (5 mM NaCl, 142 mM KCl, 1 mM  $\text{MgCl}_2$ , 2 mM EGTA, 5.6 mM glucose, 25 mM HEPES,  
665 pH 7.2) containing 2  $\mu\text{M}$  A23187, 5  $\mu\text{M}$  BIPPO or DMSO and then incubated for 30 min at  
666 37 °C. Afterwards, the supernatant was collected and further centrifuged, followed by  
667 Western blot analysis (WB). For WB, 4-20% precast polyacrylamide gel (BioRad, 4561096)  
668 were used. GRA1 and Mic2 antibody was used to label the membranes<sup>17</sup>, summarised in  
669 Supplementary Table 6. Stained membranes were imaged using Odyssey CLX-1849 (LI-  
670 COR).

671 For quantification of microneme secretion assays, this experiment was made in triplicates  
672 and run on independent membranes. Measurements were done by Image J. MIC2 secretion

673 was related to GRA1 secretion. Graphs in Fig. 3g and h are percentages of MIC2/GRA1  
674 relative to the WT in each condition.

675

676

#### 677 *Imaging processing*

678 LasX software (v. 3.4.2.183668) from Leica was used to obtain parasite imaging data and LI-  
679 COR Image Studio Software for WB images. All images and movies were processed using  
680 Fiji (ImageJ) software v.2.1.0 and/or Icy Image Processing Software 1.8.6.0. With the  
681 exception of images of parasites expressing CbEm and time-lapse videos, all widefield  
682 images were deconvolved using Huygens essential v.18.04.

683 Schemes were created using Adobe InDesign or Microsoft PowerPoint.

684

#### 685 *Software*

686 *In silico* cloning was performed using pDraw32 (AcaClone software. v. 1.1.120) and ApE. A  
687 plasmid editor (by M. Wayne Davis. V.2.0.53c) software. Sequencing results were analysed  
688 using BioEdit v.7.2. Generation of gRNAs for tagging was done in EuPaGDT<sup>31</sup>.

689

#### 690 *Statistics and reproducibility*

691 All data were plotted by Excel (Microsoft 365) or Graphpad Prism 8.2.1. Statistical analysis  
692 were carried out using Graphpad Prism. One-tail ANOVA and multiple comparison T-test  
693 were performed or unpaired two-tailed Student *t*-test as required.

694 All images presented in this manuscript are representative images. All IFAs were repeated at  
695 least 2 times with same results. In case of the screen, 3 images of every well were taken and  
696 selected candidates for further analysis were isolated and induce at least one more time to  
697 verify the phenotype observed.

698

#### 699 **Acknowledgement**

700 We thank all colleagues, who contributed antibodies and reagents for this study. In particular,  
701 we thank the Lourido lab (Whitehead Institute for Biomedical Research) in assisting with the  
702 design of the sgRNA library and many useful discussions. W.L. is funded via a CSC  
703 fellowship (201806910075). This project is funded within the DFG Priority Programme  
704 SPP2225, Project ME 2675/7-1.

#### 705 **Author contributions**

706 W.L. identified egress mutants and performed phenotypic assays for SLF and CGP. J.G.  
707 designed and performed the phenotypic screen, identified and tagged candidate genes and  
708 assisted with phenotyping. J.F.S. established and characterised the sCas9-system in *T.*  
709 *gondii*, designed the sgRNA library and analysed egress for ADF. M.G. assisted with  
710 phenotyping and analysis of parasites. J.P. assisted in experiment design and data analysis.  
711 M.M. designed and coordinated the project and experiments, analysed the data, contributed  
712 resources and wrote the paper. E.J-R. designed and coordinated the project and  
713 experiments, analysed the data, and wrote the paper.

714

#### 715 **Competing interests**

716 The authors declare no competing interests.

717

#### 718 **Figures Captions**

719 **Figure 1. Adaptation and characterisation of the splitCas9-system in *T. gondii*.** **a**, Schematic of  
720 the splitCas9-system. Transgenic parasites are generated co-expressing the two splitCas9 subunits  
721 together with a single-guide RNA (sgRNA). **b**, Analysis of RHsCas9-gap40 parasites that were treated  
722 with 50 nM rapamycin for 48h. Scale bars are 5µm. Three distinct phenotypes can be observed: the  
723 gap40 phenotype, as described previously<sup>6</sup> (top panel, asterisk); an aberrant phenotype (bottom  
724 panel); and parasites with normal IMC and GAP40 localisation (top panel, arrow). **c**, Quantification of  
725 gap40 phenotypes shown in (b) in indicated parasite strains. Parasites were induced with or without  
726 rapamycin for the indicated time and fixed 48 h post infection. Data represents three independent  
727 experiments. For each condition 100 vacuoles were counted (total n=300). Mean and standard  
728 deviation (SD) are represented. **d**, Analysis of RHsCas9-sag1 parasites that were treated with 50 nM  
729 rapamycin for 48h before fixation using indicated antibodies. Scale bars are 5µm. Two distinct  
730 phenotypes can be observed: healthy vacuoles lacking SAG1 (bottom panel, arrow); and parasites  
731 lacking SAG1 while displaying aberrant nuclear and cellular morphology (bottom panel, asterisk). **e**,  
732 Quantification of the phenotypes shown in (d). Parasites were treated with rapamycin for 1h or for the  
733 whole growth period of 48h as indicated. Data represent three independent experiments. For each  
734 condition, 100 vacuoles were counted (total n=300). Mean and SD are represented. **f**, Depiction of  
735 indicator parasites co-expressing CbEm, FNR-RFP and the sCas9-subunits. Scale bar is 5 µm. **g**,  
736 Analysis of indicator parasites expressing sgRNA targeting *sag1*. Scale bars are 5 µm. **h**, Analysis of

737 indicator parasites expressing indicated sgRNAs. IFA depicting the effect of *drpA* (RHsCas9-*drpA*), *adf*  
738 (RHsCas9-*adf*), *act1* (RHsCas9-*act1*) and *frm2* (RHsCas9-*frm2*) disruption on actin network and  
739 apicoplast segregation. Scale bars are 5  $\mu$ m. Statistics: one-sided ANOVA with Turkey's multiple test  
740 for comparison was used to analyse quantification data. ns: non-significant  $p > 0.9999$  ; colour in p  
741 values represent the condition analysed. Data presented as Mean + SD.

742 **Figure 2. Phenotypic screen for actin dynamics, apicoplast segregation and egress mutants. a,**  
743 Scheme of the experimental design. Indicator parasites, RHsCas9-CbEm-FNR-RFP, were transfected  
744 with the sgRNA library and grown in human foreskin fibroblasts (HFFs). Parasites were selected with  
745 pyrimethamine and sorted into 96-well plates. After 7 days, they were split into replica plates. Two  
746 replica plates were induced for 48h or 72h with rapamycin, before automated imaging was performed.  
747 Candidate clones were subsequently picked from non-induced replica plates. **b,** Representation of the  
748 selection of candidates in the screen. **i,** Representative images of parasites after 48h post induction  
749 (hpi). Parasites were evaluated based on their aberrant morphology or nucleus. Clones presenting  
750 aberrant phenotype in more than 70% of the screen were classified as replication phenotype. These  
751 clones were not followed up in this study. From the clones that presented a maximum of 50% of  
752 aberrant vacuoles, those presenting a change in filamentous network or in apicoplast morphology  
753 were selected for further analysis. Scale bars are 25  $\mu$ m. **ii,** Representative images of wells at 72 hpi  
754 showing potential delay or blockage in egress are shown. Top row shows clones without egress  
755 phenotype. Bottom row shows two examples of clones with a strong egress phenotype. Only clones  
756 presenting a partial or total block in egress where selected. Scale bars, 30  $\mu$ m. Finally, 2 candidates  
757 were selected for further characterisation. **iii,** Images showing the phenotype of the two identified  
758 egress mutants 48 hpi. Note that the apicoplast appears normal in both cases, while slight differences  
759 in the F-actin network, which appears more prominent and condensed, can be observed in case of  
760 TGGT1\_208420. Parasites were induced for 48 h with rapamycin before fixing and imaging. Scale  
761 bars, 5  $\mu$ m.

762 **Figure 3. Analysis of *cgp* and *sif*.** **a,** Endogenously tagged TGGT1\_240380 (*cgp*-Halo) localised at  
763 the apical tip, while TGGT1\_208420 (*sif*-Halo or *sif*-mCherry) demonstrated a dual localisation at the  
764 apical region and the residual body. Scale bar: 5  $\mu$ m. **b,** Analysis of conditional knockouts for *cgp* and  
765 *sif* using the DiCre-system. IFA depicts floxed *cgp*-Halo (loxP*cgp*-Halo) and floxed *sif*-mCherry  
766 (loxP*sif*-mCherry) induced or not with 50 nM rapamycin (Rapa). Dual labelling was performed to stain  
767 the IMC (GAP45 or IMC1) of the parasite. Scale bar, 5  $\mu$ m. **c,** Plaque assays of loxP*cgp*-Halo and  
768 loxP*sif*-mCherry parasites confirm a severe growth defect upon deletion of *sif* or *cgp*. Scale bar, 1.5  
769 mm. **d,** Invasion-attachment assay for the indicated parasites lines. Parasites were pre-treated  $\pm$  50  
770 nM rapamycin for 96 hours. Results were normalised to DiCre $\Delta ku80$  strain. For each condition, a  
771 minimum of 150 vacuoles were counted per experiment in 3 biologically independent experiments. **e,**  
772 Induced egress assay in the presence or absence of different inducers: Calcium ionophore (Ci)  
773 A23187 (2  $\mu$ M) for 5 min, BIPPO (50  $\mu$ M) for 5 min, and Propranolol (125  $\mu$ M). For each condition, a  
774 minimum of 100 vacuoles were counted per experiment in 3 biologically independent experiments. **f,**  
775 Quantification of trail deposition. Parasites were pretreated  $\pm$  50 nM rapamycin for 72 or 96 hours as  
776 indicated. Results were normalised to DiCre $\Delta ku80$  strain. Number of trails were counted in 3  
777 biologically independent replicates. **g and h,** Quantification of microneme secretion assay performed  
778 on wildtype (WT) parasites, loxP*sif*-mCherry (**g**) and loxP*cgp*-Halo (**h**) after 72 hours treatment  $\pm$  50  
779 nM rapamycin. This assay was performed in 3 biologically independent replicates. Values shown (%  
780 secretion) are the ratio MIC2/GRA1 relative to the secretion in WT parasites. Representative images  
781 are shown in Extended Data fig. 8j and 9g. Statistics in this figure: unpaired two tailed Student's *t*-test  
782 were calculated in all graphs except in 3e where one-way analysis of variance (one-way ANOVA) with  
783 Turkey's multiple comparison test was applied. Colour-coded *P* values represent the condition  
784 analysed. Data are presented as Mean + SD. Dots represent the mean for each replica (n = 3).

785 **Figure 4. SLF and CGP act at different times during egress.** **a,** Egress of parasites expressing  
786 CbEm labelling F-actin was induced with 50  $\mu$ M BIPPO and imaged with an interval of 3 seconds  
787 between frames. Yellow boxes show F-actin in intravacuolar network. Pink boxes show F-actin  
788 polymerisation centre close to the apicoplast/Golgi region (insets have enhanced contrast for better  
789 visualisation). Upper panel showing non-induced parasites as control (see movie\_S3 and S4). Yellow  
790 arrows: F-actin accumulation at the basal pole. Middle panel depicting F-actin in loxP*sif*-Halo parasites  
791 previously induced with 50 nM rapamycin. Only parasites lacking signal for SLF were recorded (see

792 movie\_S3). Bottom panel depicting F-actin in *loxPcgp*-Halo parasites previously induced with 50 nM  
793 rapamycin. Only parasites lacking signal for CGP were recorded (see movie\_S4). Blue arrow: no  
794 relocalisation of F-actin to the basal pole. Time is displayed in minutes : seconds. Scale bar, 5  $\mu$ m. **b**,  
795 Quantification of the average relative fluorescence intensity of indicated parasites after induction of  
796 egress with 50  $\mu$ M BIPPO. Graphs show the average of indicated individual measurements  $\pm$  SD. Red  
797 arrows indicate the time where the F-actin network started to depolymerise. This time was set as  $t = 0$   
798 s for all movies evaluated. Time interval between each frame is 3 seconds. Each video analysed  
799 represent a biologically independent replica (non-rapamycin induced  $n = 11$ , *cgp*-iKO  $n = 10$  and *slf*-  
800 iKO  $n = 9$ ) and a representative image is shown in panel a. **c**, Egress of parasites expressing CbEm  
801 (yellow) and SAG1 $\Delta$ GPI-dsRed (pink) was induced with 50  $\mu$ M BIPPO. Upper row images are  
802 showing non-induced *LoxPcgp*-Halo parasites, upon induction, dsRed signal diffused into the host cell,  
803 indicating lysis of parasitophorous vacuole membrane (PVM). Middle row depicting parasites lacking  
804 CGP (*LoxPcgp*-Halo + Rapa) signal after rapamycin induction. Although the PVM lysed, parasites did  
805 not move out of the cell. Bottom row depicting parasites lacking SLF signal after rapamycin induction  
806 (*LoxPslf*-Halo + Rapa), where dsRed signal is kept within the PV suggesting intact PVM. Time is  
807 displayed in minutes : seconds. Scale bar, 5  $\mu$ m. See also movie\_S5. This assay was performed in at  
808 least 3 biologically independent experiments.

809 **Figure 5. SLF is a crucial part of the signalling platform. a**, GC, UGO and CDC50.1 colocalise with  
810 SLF. Scale bar: 5  $\mu$ m. **b**, Localisation of indicated components of the signalling platform upon deletion  
811 of *slf*. Deletion of *slf-mCherry* results in mislocalisation of GC/UGO/CDC50.1. Analysis was performed  
812 96 hours post induction. Scale bar, 5  $\mu$ m. **c**, Deletion of *gc/ ugo/cdc50.1* (see also Extended Data Fig.  
813 7 for generation of conditional KOs for individual components) results in mislocalisation of SLF at 96  
814 hours post induction. Scale bar: 5  $\mu$ m. These assays were performed at least twice with same results  
815 and a representative image is here shown.

816 **Figure 6. CGP localises to the pre-conoidal rings and egress models. a**, STED microscopy of  
817 indicated parasites. Colocalisation of CGP-Halo with RNG2 or SAS6L proteins in intracellular parasites  
818 or extracellular parasites following conoid protrusion stimulation with 2  $\mu$ M calcium ionophore A23187  
819 for 10 min before fixation. White dash lines indicate parasite periphery. Scale bar, 5  $\mu$ m for intracellular  
820 parasites and 3  $\mu$ m for extracellular parasites. Scale bar of insets: 0.5  $\mu$ m. **b**, Absence of CGP did not  
821 affect the localisation of RNG2 and SAS6L. Scale bar, 5  $\mu$ m. Images in a and b were taken in at least  
822 3 biologically independent experiments with same results and a representative image of each is  
823 shown. **c**, Block of egress caused by deletion of SLF, CGP and ADF (see Extended Data Fig.3) is  
824 intrinsically linked to the disassembly of the F-actin network. **1-3**) Natural egress process in a wildtype  
825 parasite. **1**) At the start of the egress the signalling platform consisting of CDC50.1, GC, UGO and  
826 SLF, localised at the plasma membrane of the apical tip and the intravacuolar network (IVN), initiates  
827 a cascade leading to egress. Zoom in boxes: yellow arrows indicate the position of the signalling  
828 platform at the apical tip and residual body. Purple arrow indicates the position of CGP at the conoid of  
829 the parasites. **2**) As a first step towards egress, the IVN disassembles, which coincides with lysis of  
830 the PVM. **3**) F-actin accumulates at the basal end of the parasite and motility is initiated. **4**) In the  
831 absence of SLF, the signalling platform is mislocalised, resulting in early block of egress. No  
832 disassembly of the intravacuolar network or PVM lysis occurs. **5**) Depletion of actin regulatory proteins  
833 results in stabilisation of the network. Although parasites lyse the PVM and initiate motility, the network  
834 keeps connecting individual parasites resulting in delayed or blocked egress (see Figure S3 and <sup>11</sup>). **6**)  
835 Deletion of *cgp* results in a late block of egress. The signalling cascade appears intact, leading to  
836 disassembly of the intravacuolar network and lysis of the PVM. Instead, no relocation of F-actin to the  
837 basal pole can occur and motility is not initiated.

838

839

840

841 **Data availability**

842 All imaging data generated and used for this paper are available from the authors on  
843 reasonable request. The source data are provided as a Source Data file. Expression  
844 constructs and parasite strains have been deposited in Addgene (<https://www.addgene.org/>).  
845 Information on *T.gondii* genes and proteins were obtained in ToxoDB (release 30 to 56).  
846 Data obtained from sequencing have been deposited in SRA  
847 (<https://www.ncbi.nlm.nih.gov/sra>): Bioproject ID: PRJNA821386

848

849 **References**

- 850 1 Sidik, S. M. *et al.* A Genome-wide CRISPR Screen in Toxoplasma Identifies Essential  
851 Apicomplexan Genes. *Cell* **166**, 1423-1435.e1412, doi:10.1016/j.cell.2016.08.019 (2016).
- 852 2 Serpeloni, M. *et al.* UAP56 is a conserved crucial component of a divergent mRNA export  
853 pathway in Toxoplasma gondii. *Molecular microbiology* **102**, 672-689, doi:  
854 10.1111/mmi.13485. (2016).
- 855 3 Zetsche, B., Volz, S. E. & Zhang, F. A split-Cas9 architecture for inducible genome editing and  
856 transcription modulation. *Nature biotechnology* **33**, 139-142, doi:10.1038/nbt.3149 (2015).
- 857 4 Periz, J. *et al.* Toxoplasma gondii F-actin forms an extensive filamentous network required for  
858 material exchange and parasite maturation. *eLife* **6**, doi:10.7554/eLife.24119 (2017).
- 859 5 Kim, K., Soldati, D. & Boothroyd, J. C. Gene replacement in Toxoplasma gondii with  
860 chloramphenicol acetyltransferase as selectable marker. *Science (New York, N.Y.)* **262**, 911-  
861 914, doi:10.1126/science.8235614 (1993).
- 862 6 Harding, C. R. *et al.* Gliding Associated Proteins Play Essential Roles during the Formation of  
863 the Inner Membrane Complex of Toxoplasma gondii. *PLoS pathogens* **12**, e1005403,  
864 doi:10.1371/journal.ppat.1005403 (2016).
- 865 7 Striepen, B. *et al.* The plastid of Toxoplasma gondii is divided by association with the  
866 centrosomes. *The Journal of cell biology* **151**, 1423-1434, doi:10.1083/jcb.151.7.1423 (2000).
- 867 8 van Dooren, G. G. *et al.* A novel dynamin-related protein has been recruited for apicoplast  
868 fission in Toxoplasma gondii. *Current biology : CB* **19**, 267-276,  
869 doi:10.1016/j.cub.2008.12.048 (2009).
- 870 9 Andenmatten, N. *et al.* Conditional genome engineering in Toxoplasma gondii uncovers  
871 alternative invasion mechanisms. *Nature methods* **10**, 125-127, doi:10.1038/nmeth.2301  
872 (2013).
- 873 10 Del Rosario, M. *et al.* Apicomplexan F-actin is required for efficient nuclear entry during host  
874 cell invasion. *EMBO Rep*, e48896, doi:10.15252/embr.201948896 (2019).
- 875 11 Stortz, J. F. *et al.* Formin-2 drives polymerisation of actin filaments enabling segregation of  
876 apicoplasts and cytokinesis in Plasmodium falciparum. *eLife* **8**, doi:10.7554/eLife.49030  
877 (2019).
- 878 12 Mehta, S. & Sibley, L. D. Actin depolymerizing factor controls actin turnover and gliding  
879 motility in Toxoplasma gondii. *Molecular biology of the cell* **22**, 1290-1299,  
880 doi:10.1091/mbc.E10-12-0939 (2011).
- 881 13 Plattner, F. *et al.* Toxoplasma profilin is essential for host cell invasion and TLR11-dependent  
882 induction of an interleukin-12 response. *Cell host & microbe* **3**, 77-87,  
883 doi:10.1016/j.chom.2008.01.001 (2008).
- 884 14 Sidik, S. M., Huet, D. & Lourido, S. CRISPR-Cas9-based genome-wide screening of Toxoplasma  
885 gondii. *Nature protocols* **13**, 307-323, doi:10.1038/nprot.2017.131 (2018).

886 15 Aquilini, E. *et al.* An Alveolata secretory machinery adapted to parasite host cell invasion. *Nat*  
887 *Microbiol* **6**, 425-434, doi:10.1038/s41564-020-00854-z (2021).

888 16 Sidik, S. M. *et al.* A Genome-wide CRISPR Screen in Toxoplasma Identifies Essential  
889 Apicomplexan Genes. *Cell* **166**, 1423-1435 e1412, doi: 10.1016/j.cell.2016.08.019. (2016).

890 17 Bisio, H., Lunghi, M., Brochet, M. & Soldati-Favre, D. Phosphatidic acid governs natural egress  
891 in Toxoplasma gondii via a guanylate cyclase receptor platform. *Nature microbiology* **4**, 420-  
892 428, doi:10.1038/s41564-018-0339-8 (2019).

893 18 Barylyuk, K. *et al.* A Comprehensive Subcellular Atlas of the Toxoplasma Proteome via  
894 hyperLOPIT Provides Spatial Context for Protein Functions. *Cell host & microbe* **28**, 752-  
895 766.e759, doi:10.1016/j.chom.2020.09.011 (2020).

896 19 Beck, J. R. *et al.* A novel family of Toxoplasma IMC proteins displays a hierarchical  
897 organization and functions in coordinating parasite division. *PLoS pathogens* **6**, e1001094,  
898 doi:10.1371/journal.ppat.1001094 (2010).

899 20 Andenmatten, N. *et al.* Conditional genome engineering in Toxoplasma gondii uncovers  
900 alternative invasion mechanisms. *Nature methods* **10**, 125-127, doi: 10.1038/nmeth.2301.  
901 (2013).

902 21 Bullen, H. E., Bisio, H. & Soldati-Favre, D. The triumvirate of signaling molecules controlling  
903 Toxoplasma microneme exocytosis: Cyclic GMP, calcium, and phosphatidic acid. *PLoS Pathog*  
904 **15**, e1007670, doi:10.1371/journal.ppat.1007670 (2019).

905 22 MacRae, J. I. *et al.* Mitochondrial metabolism of glucose and glutamine is required for  
906 intracellular growth of Toxoplasma gondii. *Cell Host Microbe* **12**, 682-692,  
907 doi:10.1016/j.chom.2012.09.013 (2012).

908 23 Fuks, J. M. *et al.* GABAergic signaling is linked to a hypermigratory phenotype in dendritic  
909 cells infected by Toxoplasma gondii. *PLoS Pathog* **8**, e1003051,  
910 doi:10.1371/journal.ppat.1003051 (2012).

911 24 Koreny, L. *et al.* Molecular characterization of the conoid complex in Toxoplasma reveals its  
912 conservation in all apicomplexans, including Plasmodium species. *PLoS biology* **19**, e3001081,  
913 doi:10.1371/journal.pbio.3001081 (2021).

914 25 Fisch, D. *et al.* Defining host-pathogen interactions employing an artificial intelligence  
915 workflow. *eLife* **8**, doi:10.7554/eLife.40560 (2019).

916 26 Moen, E. *et al.* Deep learning for cellular image analysis. *Nat Methods* **16**, 1233-1246,  
917 doi:10.1038/s41592-019-0403-1 (2019).

918 27 Jimenez-Ruiz, E., Wong, E. H., Pall, G. S. & Meissner, M. Advantages and disadvantages of  
919 conditional systems for characterization of essential genes in Toxoplasma gondii.  
920 *Parasitology* **141**, 1390-1398, doi:10.1017/s0031182014000559 (2014).

921 28 Meissner, M., Schluter, D. & Soldati, D. Role of Toxoplasma gondii myosin A in powering  
922 parasite gliding and host cell invasion. *Science (New York, N.Y.)* **298**, 837-840,  
923 doi:10.1126/science.1074553 (2002).

924 29 Sidik, S. M., Hackett, C. G., Tran, F., Westwood, N. J. & Lourido, S. Efficient genome  
925 engineering of Toxoplasma gondii using CRISPR/Cas9. *PloS one* **9**, e100450,  
926 doi:10.1371/journal.pone.0100450 (2014).

927 30 Donald, R. G., Carter, D., Ullman, B. & Roos, D. S. Insertional tagging, cloning, and expression  
928 of the Toxoplasma gondii hypoxanthine-xanthine-guanine phosphoribosyltransferase gene.  
929 Use as a selectable marker for stable transformation. *The Journal of biological chemistry* **271**,  
930 14010-14019, doi:10.1074/jbc.271.24.14010 (1996).

931 31 Peng, D. & Tarleton, R. EuPaGDT: a web tool tailored to design CRISPR guide RNAs for  
932 eukaryotic pathogens. *Microb Genom* **1**, e000033, doi:10.1099/mgen.0.000033 (2015).

933 32 Curt-Varesano, A., Braun, L., Ranquet, C., Hakimi, M. A. & Bougdour, A. The aspartyl protease  
934 TgASP5 mediates the export of the Toxoplasma GRA16 and GRA24 effectors into host cells.  
935 *Cell Microbiol* **18**, 151-167, doi:10.1111/cmi.12498 (2016).

936 33 Hunt, A. *et al.* Differential requirements for cyclase-associated protein (CAP) in actin-  
937 dependent processes of Toxoplasma gondii. *eLife* **8**, doi:10.7554/eLife.50598 (2019).

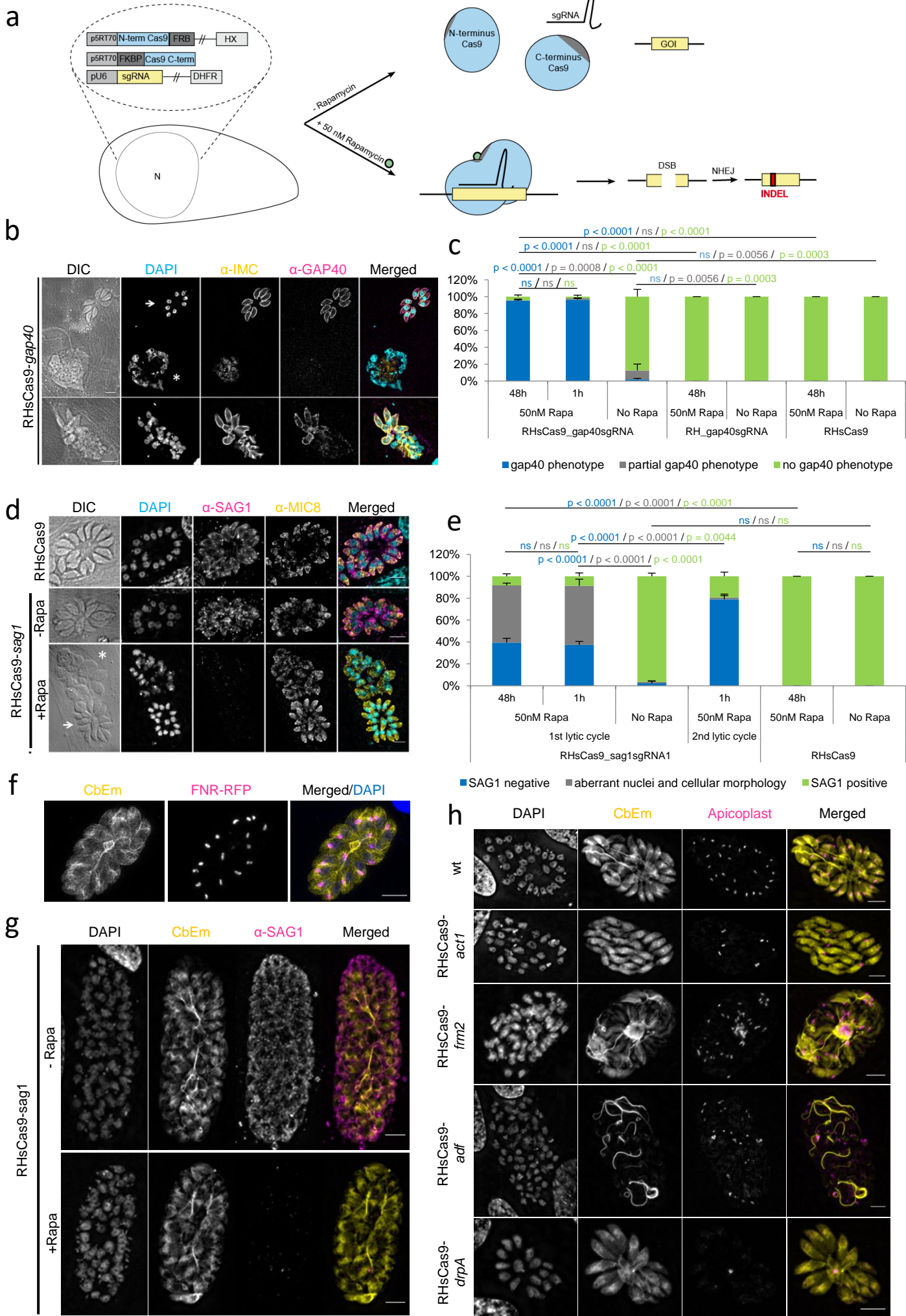


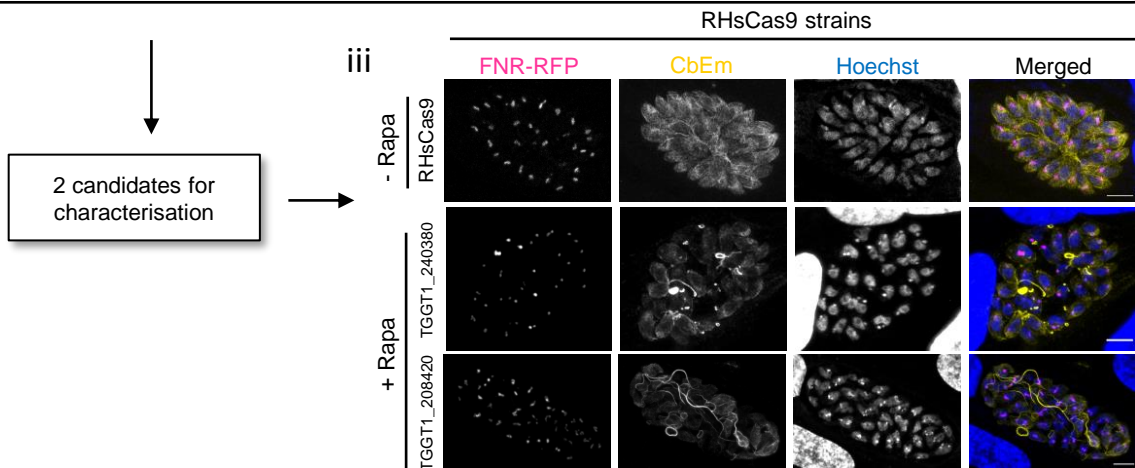
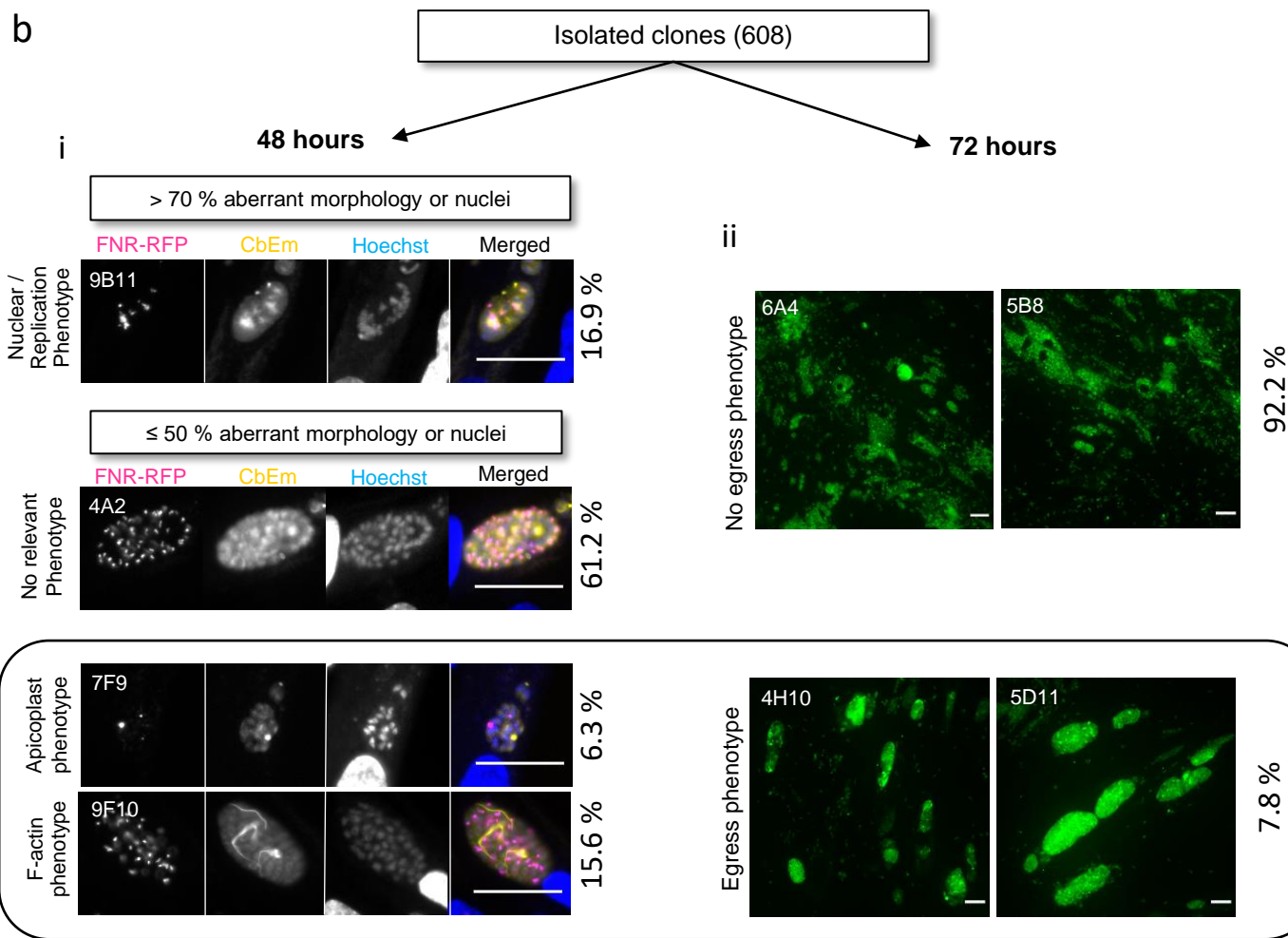
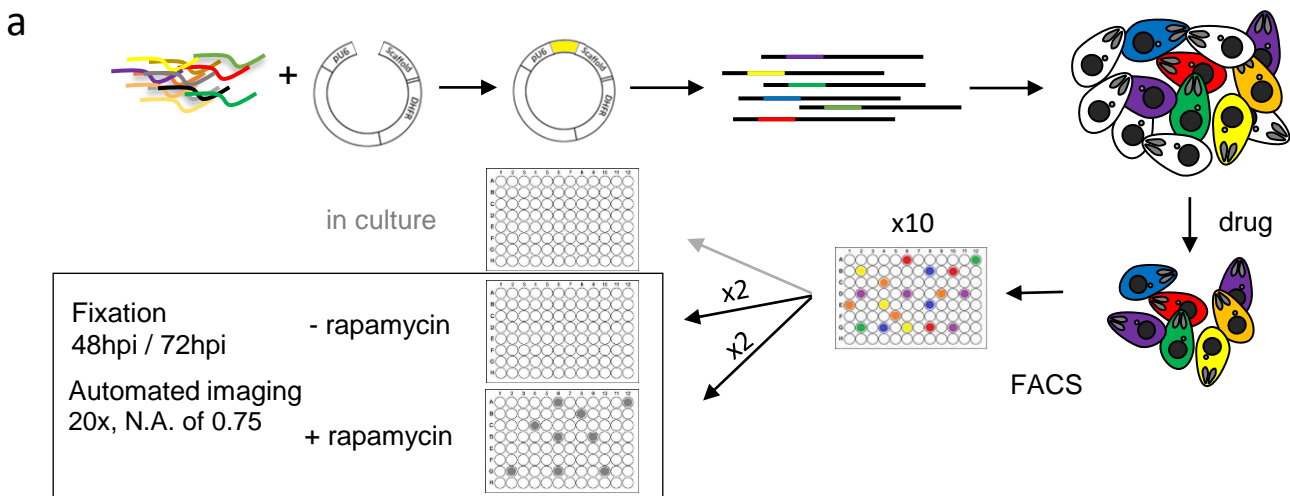
938 34 Egarter, S. *et al.* The toxoplasma Acto-MyoA motor complex is important but not essential for  
939 gliding motility and host cell invasion. *PloS one* **9**, e91819, doi:10.1371/journal.pone.0091819  
940 (2014).

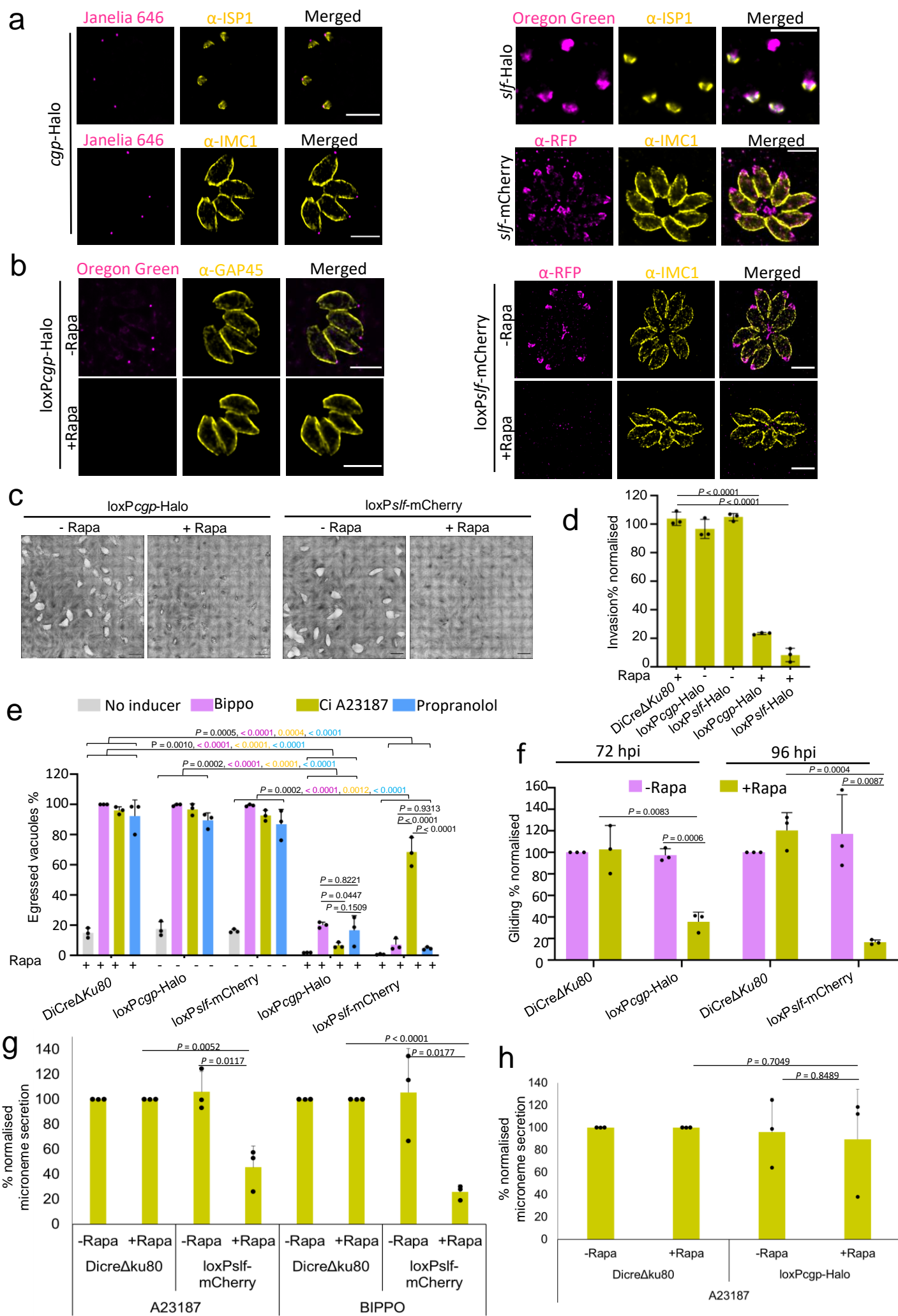
941 35 Periz, J. *et al.* A highly dynamic F-actin network regulates transport and recycling of  
942 micronemes in *Toxoplasma gondii* vacuoles. *Nature communications* **10**, 4183,  
943 doi:10.1038/s41467-019-12136-2 (2019).

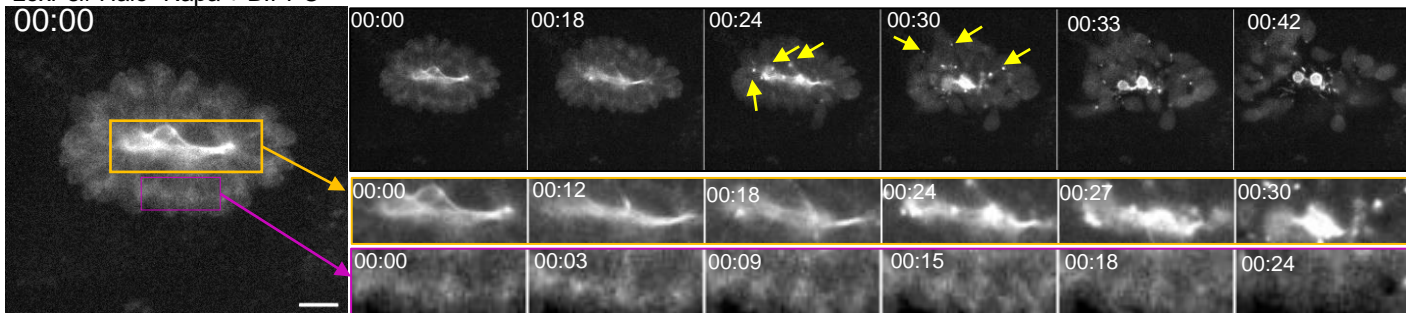
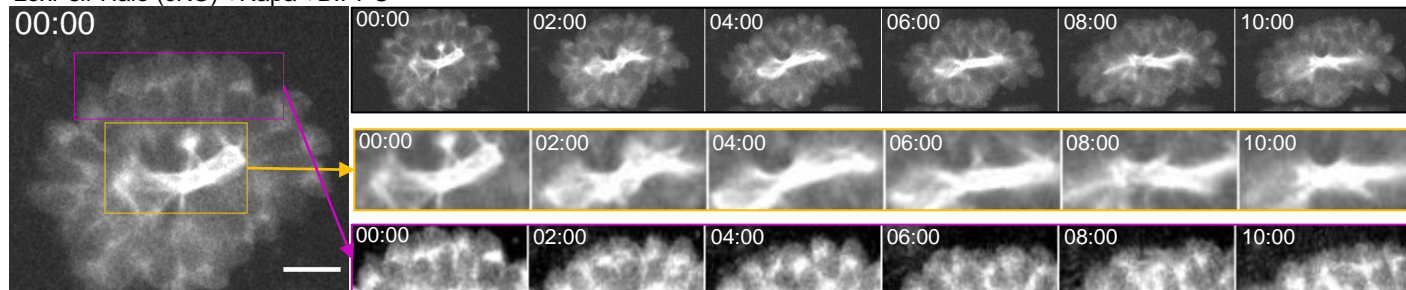
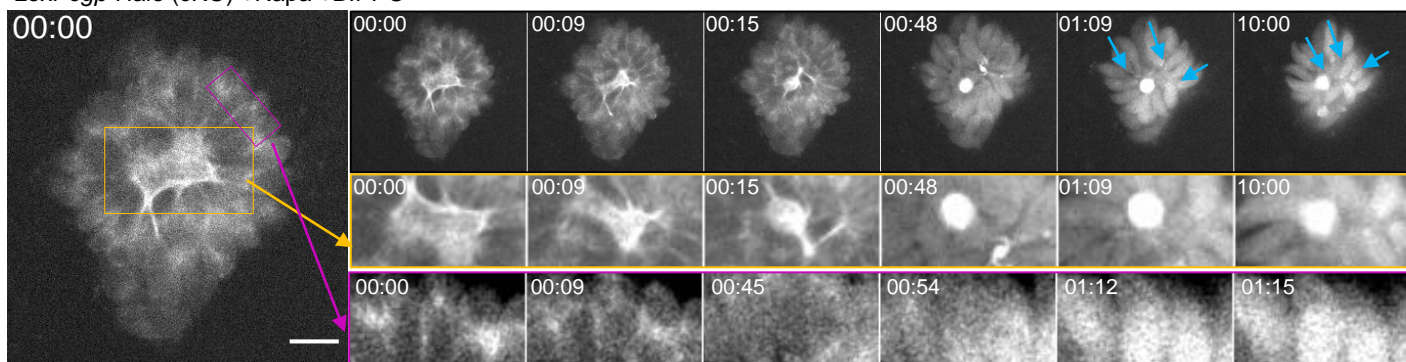
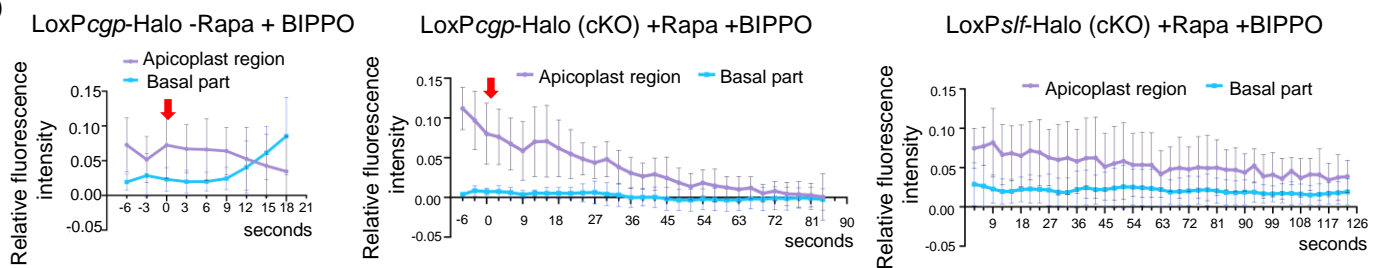
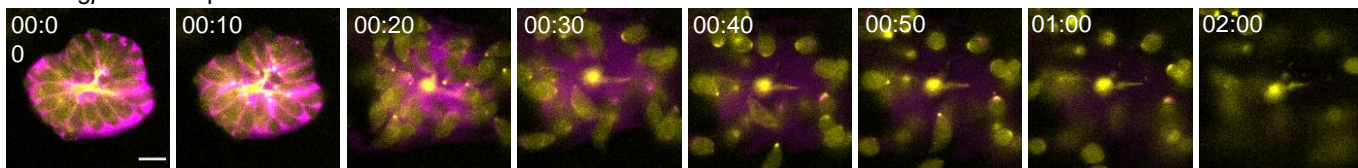
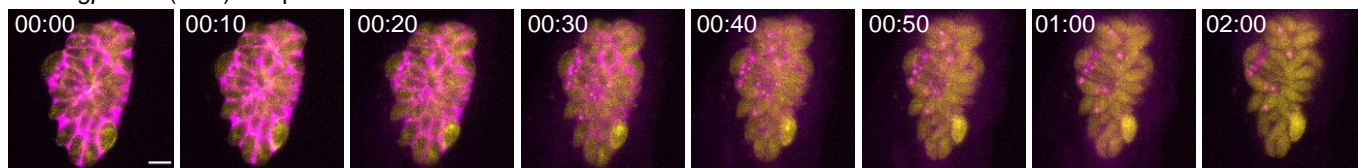
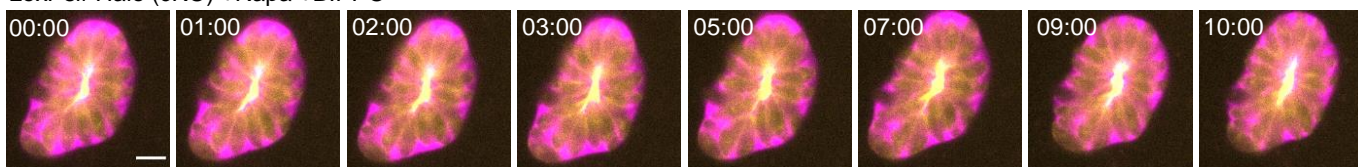
944

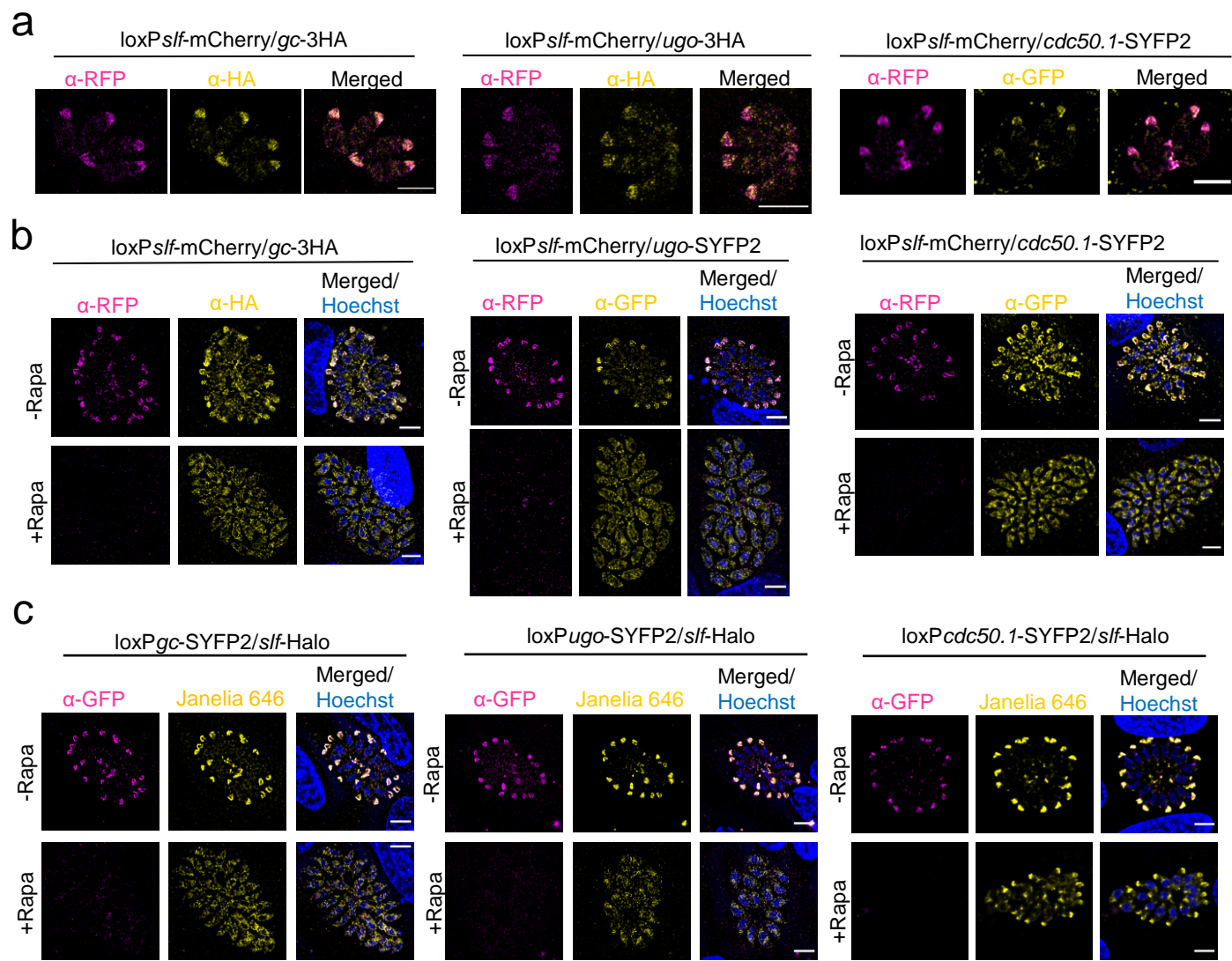
945

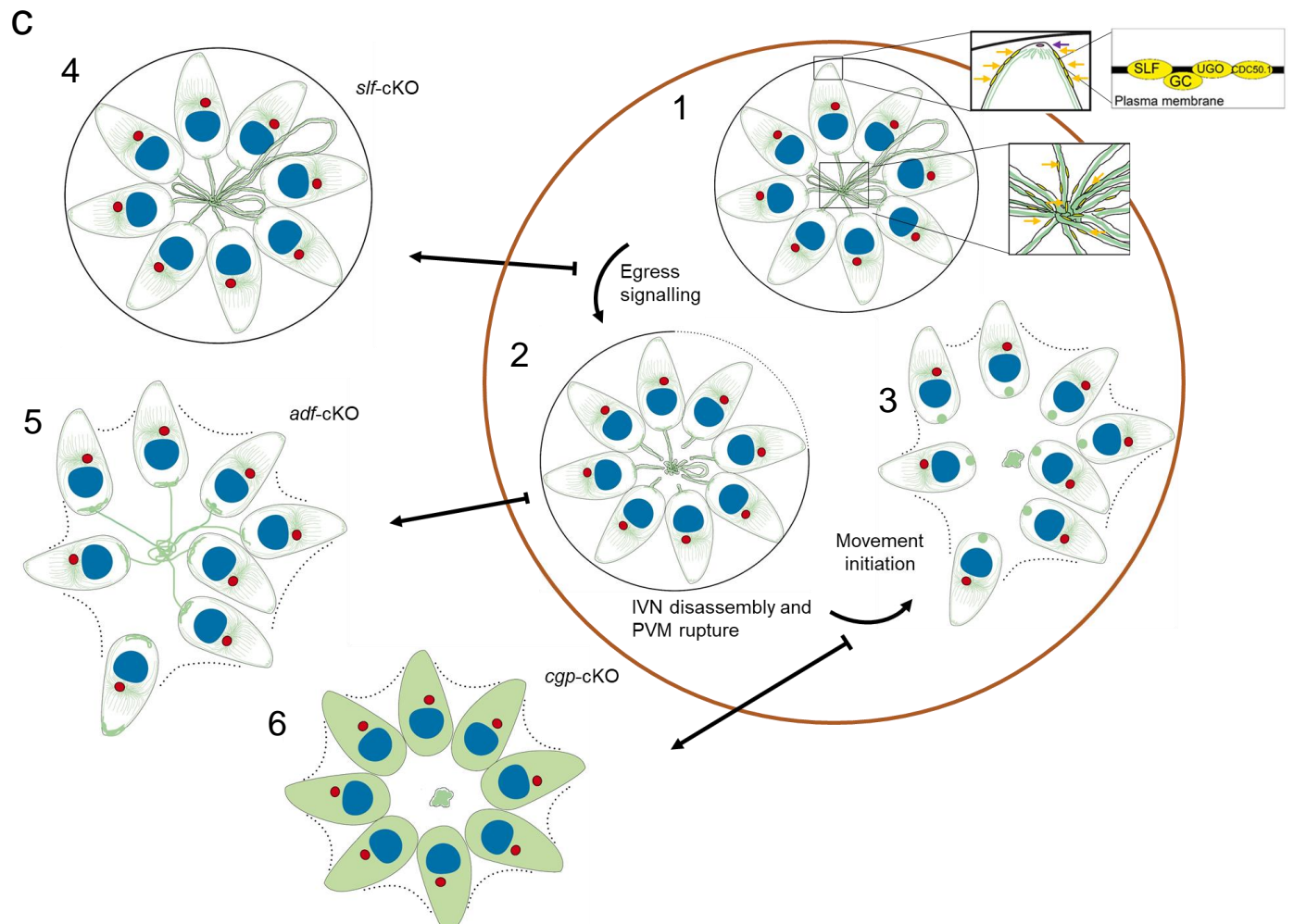
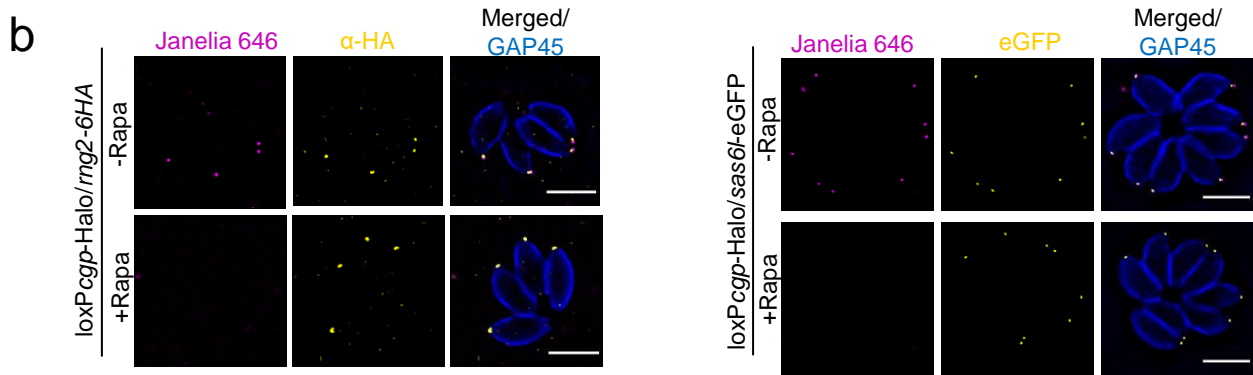
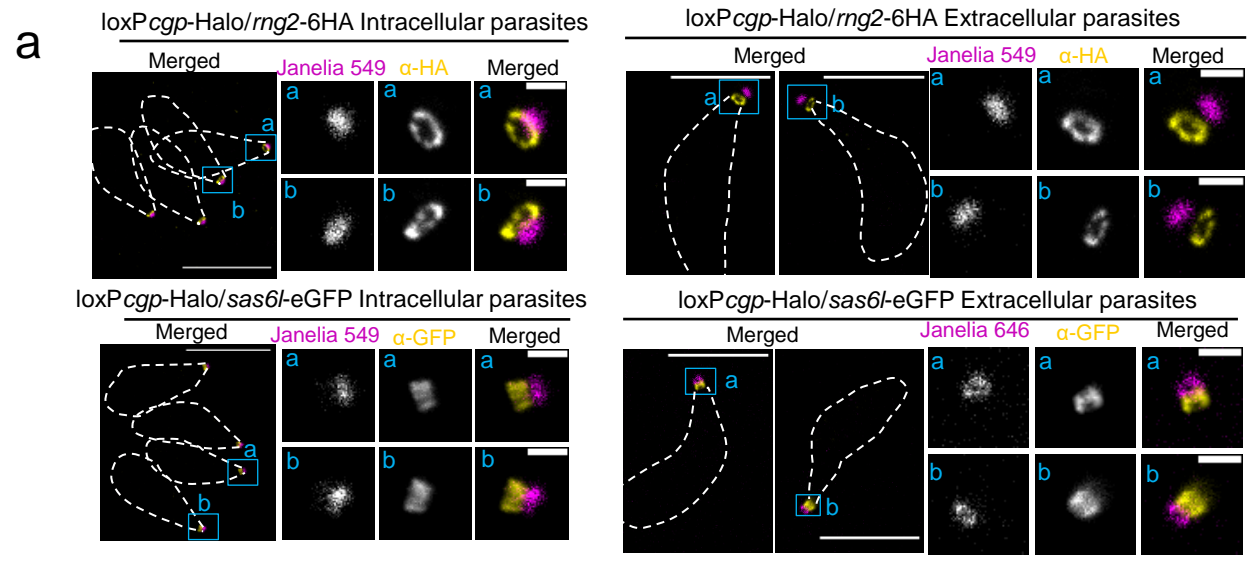


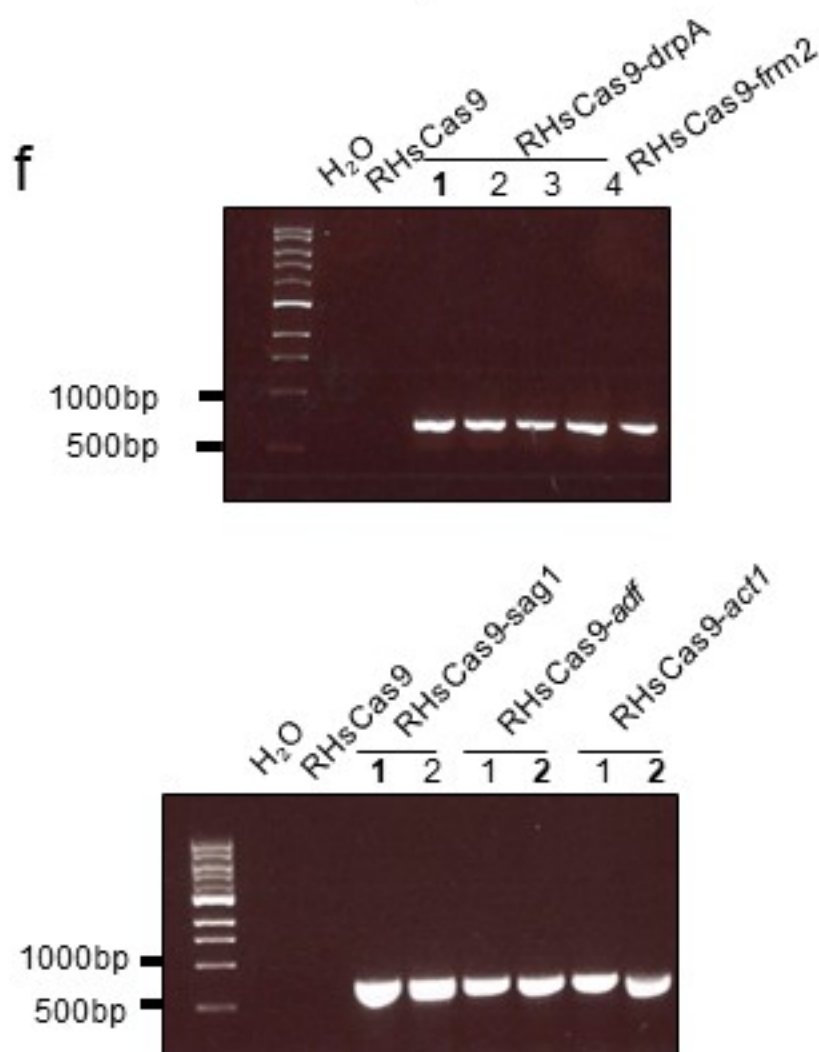
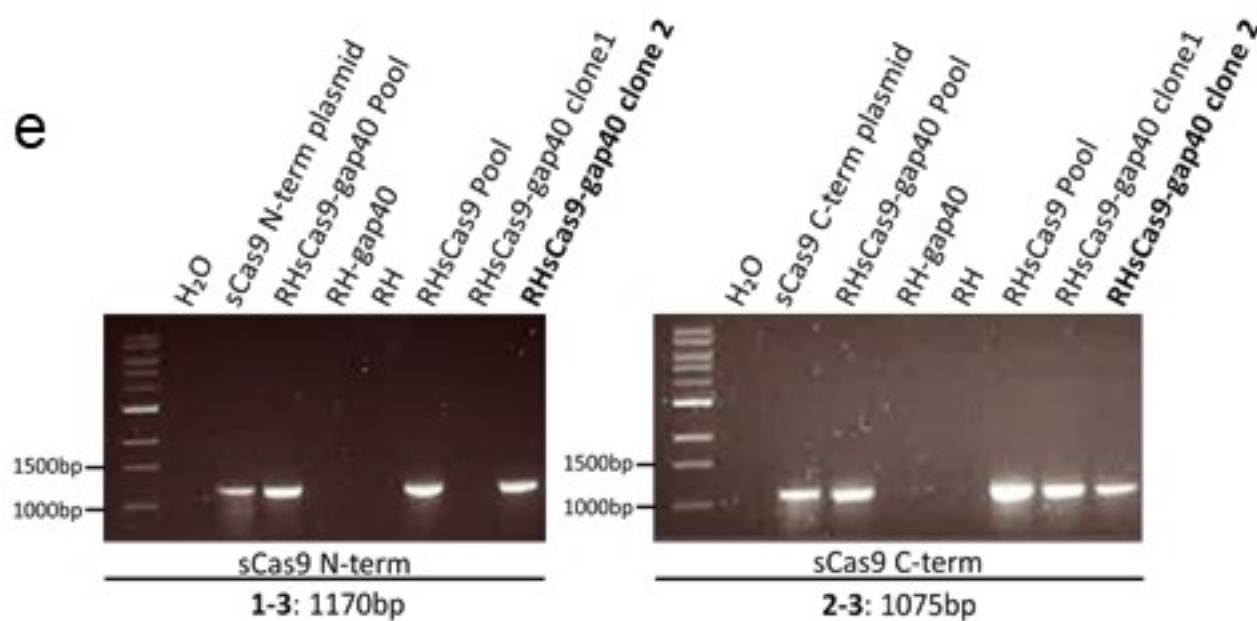
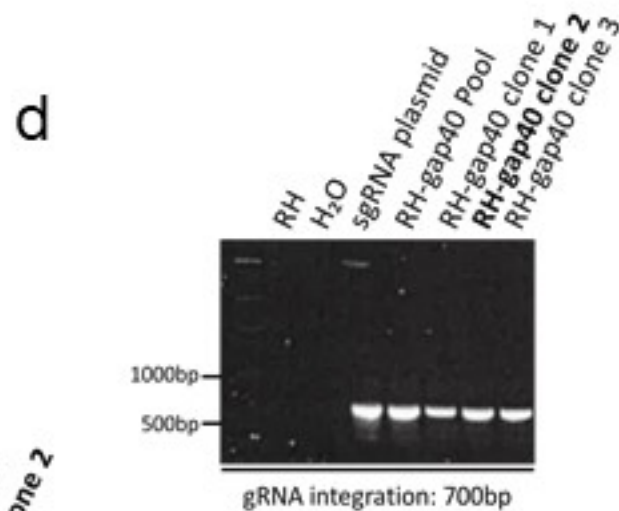
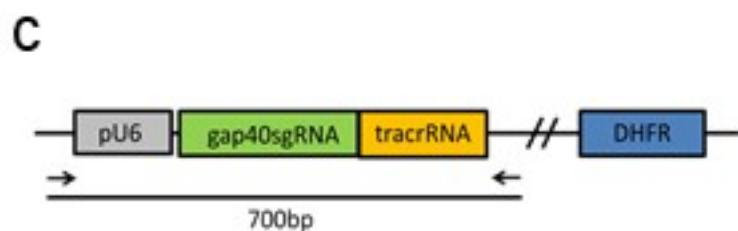
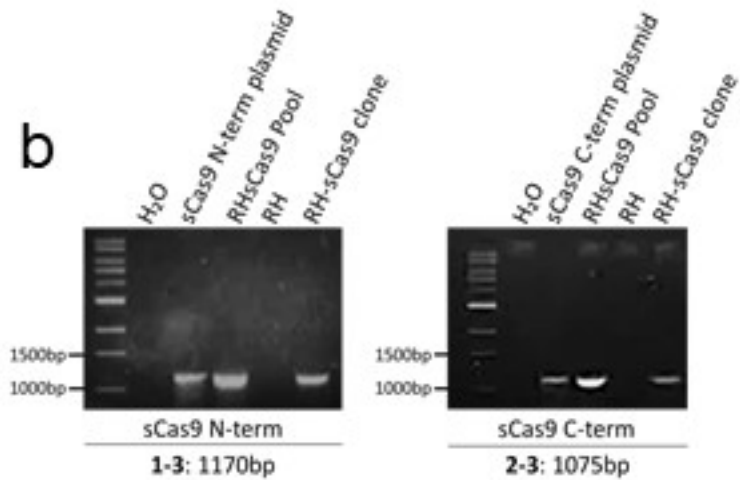
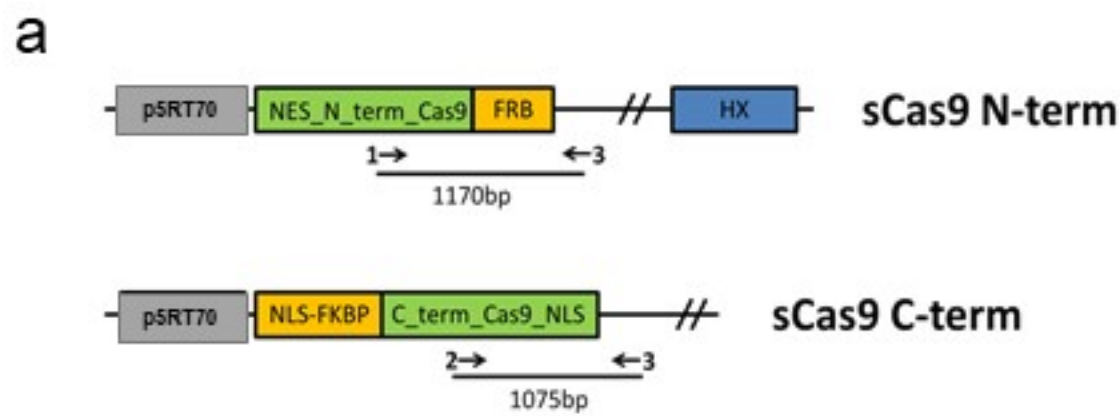




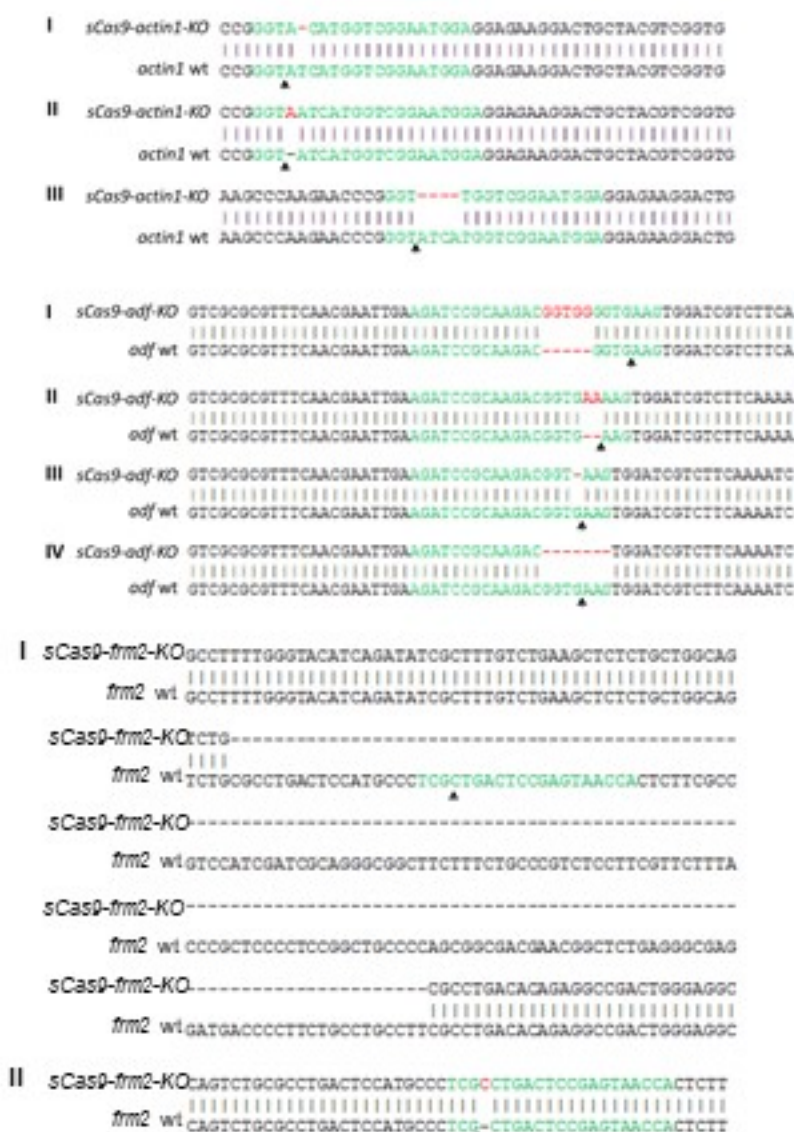
**a**LoxPs/*f*-Halo -Rapa + BIPPOLoxPs/*f*-Halo (cKO) +Rapa +BIPPOLoxP*cgp*-Halo (cKO) +Rapa +BIPPO**b****c**LoxP*cgp*-Halo -Rapa + BIPPOLoxP*cgp*-Halo (cKO) +Rapa +BIPPOLoxPs/*f*-Halo (cKO) +Rapa +BIPPO



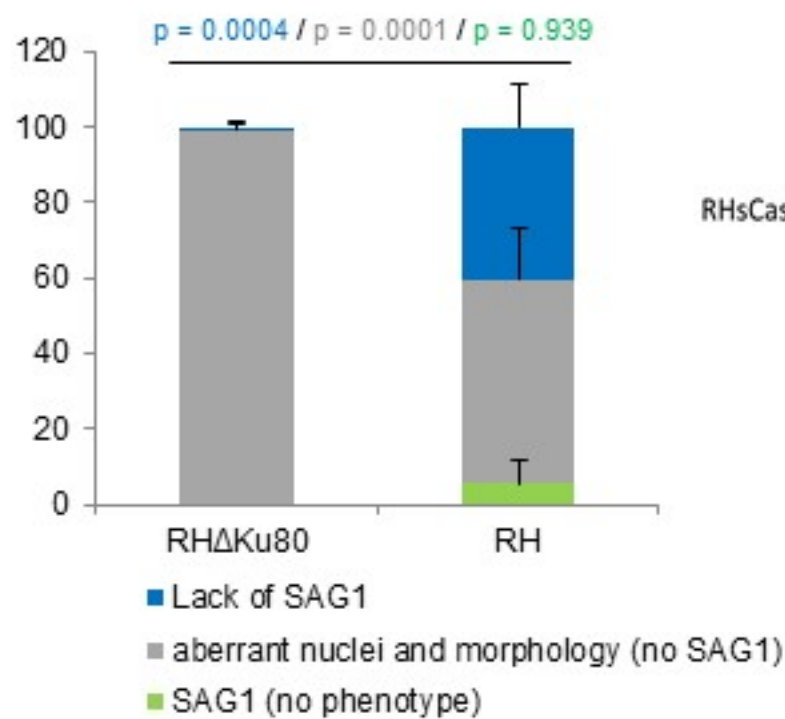




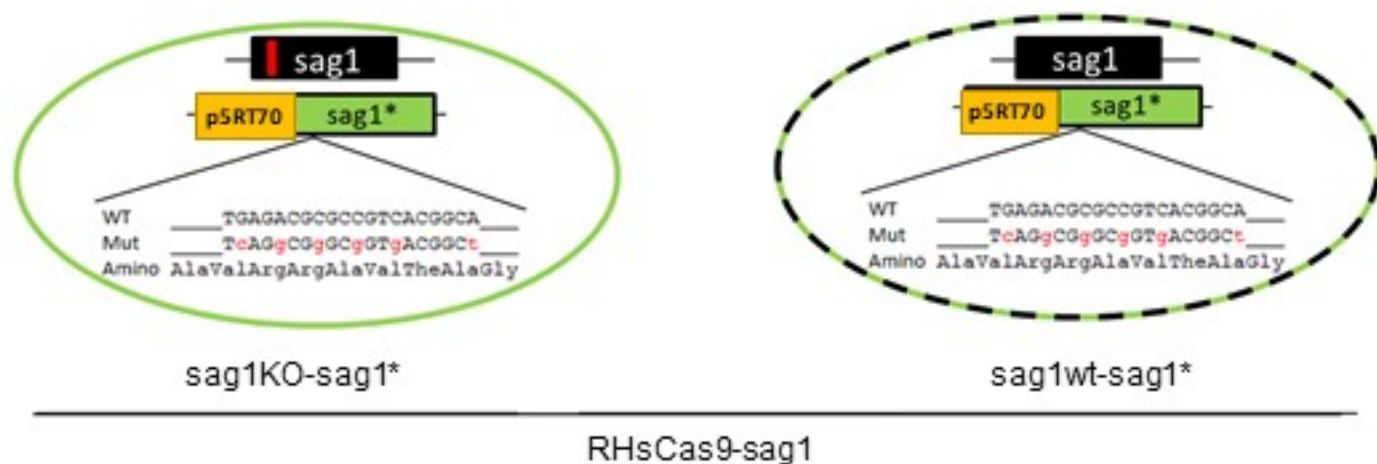
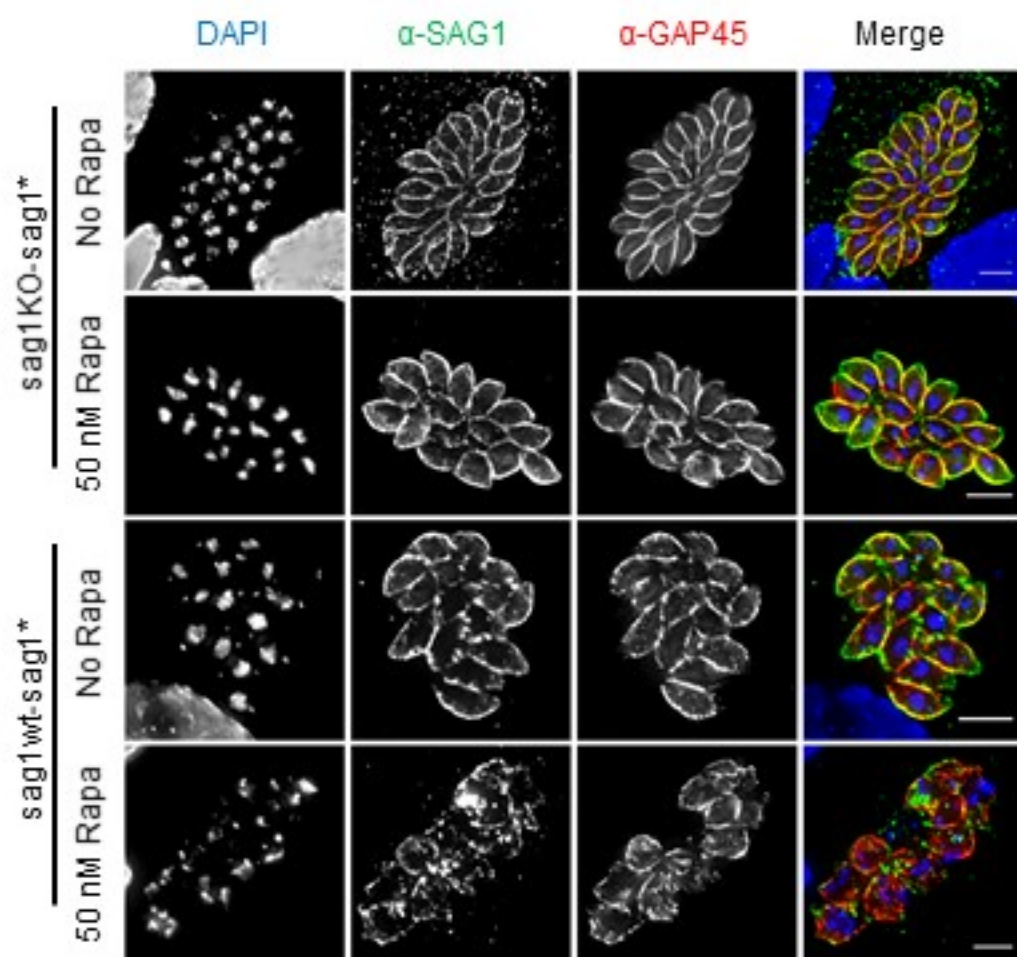
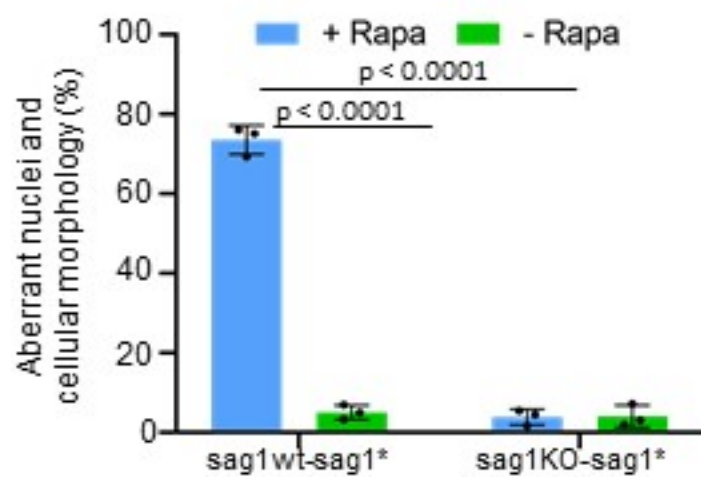
**g**





**a****b**

*sag1* wt AAGGCAGT**AGACGCGCCGTCAC**-GGCAGGGGT  
 RHsCas9-Δhx-*sag1*-1-KO AAGGCAGT**GGCAGGGGT**

**c****d****e****f**